Optimization of low-carbon lightweight foamed concrete using ground circulating fluidized bed fly ash

Zhang, Hongzhi; Liang, Quping; Shao, Mingyang; Jiang, Nengdong; Ma, Wenqiang; Ge, Zhi; Šavija, Branko

DOI
10.1016/j.jclepro.2025.144697

Publication date
2025

Document Version
Final published version

Published in
Journal of Cleaner Production

Journal of Cleaner Production 489 (2025) 144697

Contents lists available at ScienceDirect

Journal of Cleaner Production

journal homepage: www.elsevier.com/locate/jclepro

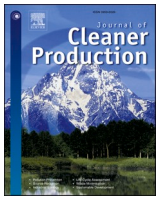

Optimization of low-carbon lightweight foamed concrete using ground circulating fluidized bed fly ash

Hongzhi Zhang [a], Quping Liang [a], Mingyang Shao [a], Nengdong Jiang [a], Wenqiang Ma [a], Zhi Ge [a,*], Branko Šavija [b]

[a] School of Qilu Transportation, Shandong University, Jinan, 250002, PR China
[b] Microlab, Faculty of Civil Engineering and Geosciences, Delft University of Technology, 2628 CN, Delft, the Netherlands

ARTICLE INFO

Handling Editor: Jin-Kuk Kim

1. Introduction

Lightweight foamed concrete (LFC) is a porous material generally composed of a certain proportion of cementitious materials, foam and water (Gencel et al., 2022). LFC is usually produced in densities of 300–1920 kg/m^3 by adjusting the foam dosage (Tran et al., 2022). The performance of LFC varies with the air-void volume, which is typically within the 30%–70% range (Zhou and Su, 2023). LFC is widely employed in engineering fields, including roadbed widening, soft foundation replacement, and back filling behind abutments (Le et al., 2022).

The main constituent of LFC is cement. The CO_2 emission in cement production process is high, reported by Schneider et al. (2023), which accounts for approximately 8% of global CO_2 emissions. Using supplementary cementitious materials (SCMs) has been considered as an effective means of reducing CO_2 emissions associated with LFC production (Gupta and Chaudhary, 2022). In addition to reducing cement consumption, the incorporation of SCMs can enhance the properties of LFC. To improve the durability of LFC, Yang et al. (2022) found that replacing 10% of cement with fly ash by mass reduced the water absorption of LFC by 4.8% while avoiding the increase of density. Golaszewska and Giergiczny (2021) found that slag and limestone reduced the hydration heat of LFC and therefore improved the temperature cracking resistance. Wang et al. (2020) reported that the incorporation of silica fume in the liquid foaming stage could improve the foam stability, thus optimizing the fine cellular structure. The reason is that the interaction of silica fume with the foaming agent contributes to the generation of three phase (solid-liquid-gas) foam with higher stability than liquid-gas two-phase foam. In addition, metakaolin (Shi et al., 2021), zeolite powder (Karakurt et al., 2010), rice husk ash (Aravind et al., 2020), etc. have also been reported to bring benefits to LFC while reducing CO_2 emission.

The solid wastes on industrial, agricultural, quarrying, and construction sites are generated in billions of tons every year, and their amount is growing. The resource wastage, environment pollution and storage expense have exerted tremendous pressure on governments (Ji et al., 2023; Wang et al., 2024a). An increasing number of scholars are investigating the conversion of waste into construction materials, with purpose of reducing the reliance of building materials on natural resources (Ji et al., 2024; Liu and Wang, 2024). For this end, LFC presents a satisfactory avenue for large-scale consumption of solid wastes (Shah et al., 2021; Yao et al., 2019, 2023a).

Circulating fluidized bed fly ash (CFBFA) is generated by inferior coal such as coal gangue and lignite combusted in circulating fluidized bed (CFB) boiler (Zhang et al., 2021, 2023c). CFB in-furnace desulphurization has been applied as a kind of clean coal combustion technology for its advantages of wide combustion adaptability, high combustion efficiency, low nitrogen and sulfur emission, and low cost (Jia et al., 2022). As a result, the proportion of by-product CFBFA in solid waste is increasing rapidly (He et al., 2021). Its production in China, Europe, and the United States exceeds 280 million tons (Duan et al., 2018), 1.5 million tons (Ohenoja et al., 2019), and 14 million tons (Zahedi and Rajabipour, 2019) per year, respectively. Ref (Shen, 2009; Cho et al., 2021; Zhou et al., 2020). reported that its pozzolanic activity and hydraulicity endow CFBFA with the ability to serve as an SCM. Zhou et al. (2020) reported that CFBFA has a stronger pozzolanic activity than

* Corresponding author.
E-mail address: zhige@sdu.edu.cn (Z. Ge).

https://doi.org/10.1016/j.jclepro.2025.144697
Received 27 September 2024; Received in revised form 7 December 2024; Accepted 5 January 2025
Available online 7 January 2025

Table 1
Chemical composition (mass fraction, %).

Component	SiO_2	Al_2O_3	Fe_2O_3	CaO	MgO	SO_3	TiO_2
Cement	20.82	4.48	3.33	63.51	2.82	2.25	0
CFBFA	44.63	31.91	9.38	4.67	0	4.78	1.31

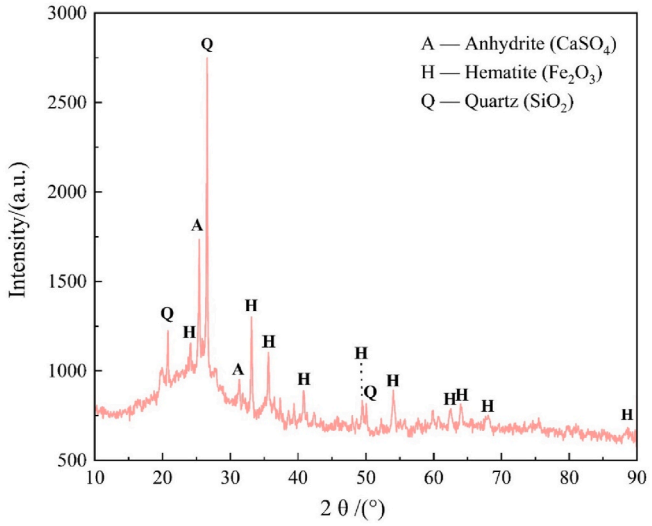

Fig. 1. XRD pattern of CFBFA.

pulverized coal combustion fly ash (PFA) because the active SiO_2 and Al_2O_3 of CFBFA dissolves more readily and produces more hydration products. However, in consequence of the low combustion temperature (800–900 °C) and the desulfurization process, CFBFA has a looser structure, higher sulfur and calcium content, as well as greater loss on ignition than PFA (Li et al., 2021b; Yoon et al., 2023; Liu et al., 2020). Difficulties like high water requirement and high expansion hinder the utilization of CFBFA which contains a lot of unstable components (f-CaO and II-$CaSO_4$) (Cheng et al., 2020). Yin et al. (2015) reported that the optimal dosage of CFBFA in cement is 30% and that an additional 5% silica fume or 10% ultrafine fly ash further improves the water demand, setting time, and strength. Cheng et al. (2023) utilized CFBFA in LFC as the artificial air bubbles could accommodate the expansion of CFBFA. It was reported that LFC with 66.7% CFBFA demonstrated satisfactory volume stability and strength. Mineral admixtures (Zhang et al., 2022c), alkali activators (Chen et al., 2020), and mechanical activation (Du et al., 2022; Li et al., 2021a; Paaver et al., 2021) have been applied to improve the performance of CFBFA. Zheng et al. (2023) compared the hydration characteristics of PFA, CFBFA, and ground CFBFA (GCFBFA) resulting in an ordering of their pozzolanic activities as GCFBFA, CFBFA, and PFA. It was proposed that grinding can destroy the core-shells of II-$CaSO_4$ and f-CaO, accelerating the mutual excitation of cement and CFBFA, thus promoting the large-scale application of CFBFA. However, increasing but still limited work has been conducted concerning the replacement of cement by GCFBFA in LFC, which contributes to the cleaner production of LFC and consumption of CFBFA. The influence of GCFBFA on the properties of LFC such as workability, mechanical properties and durability, as well as the dosage limitations in LFC for subgrade filling, are still unclear.

To this end, the current investigation applies GCFBFA as an SCM in preparing low-carbon LFC for subgrade filling. Effects of GCFBFA substitution on the setting time, mechanical properties, hydration products, hydration heat and rheological properties of binder were investigated. Afterwards, the effect of wet density and GCFBFA substitution on the fresh properties, mechanical properties, air-void structure, water stability, freeze-thaw resistance and life cycle assessment of LFC was further explored. This study presents a theoretical foundation for the large-scale implementation of CFBFA in low-carbon LFC for engineering application.

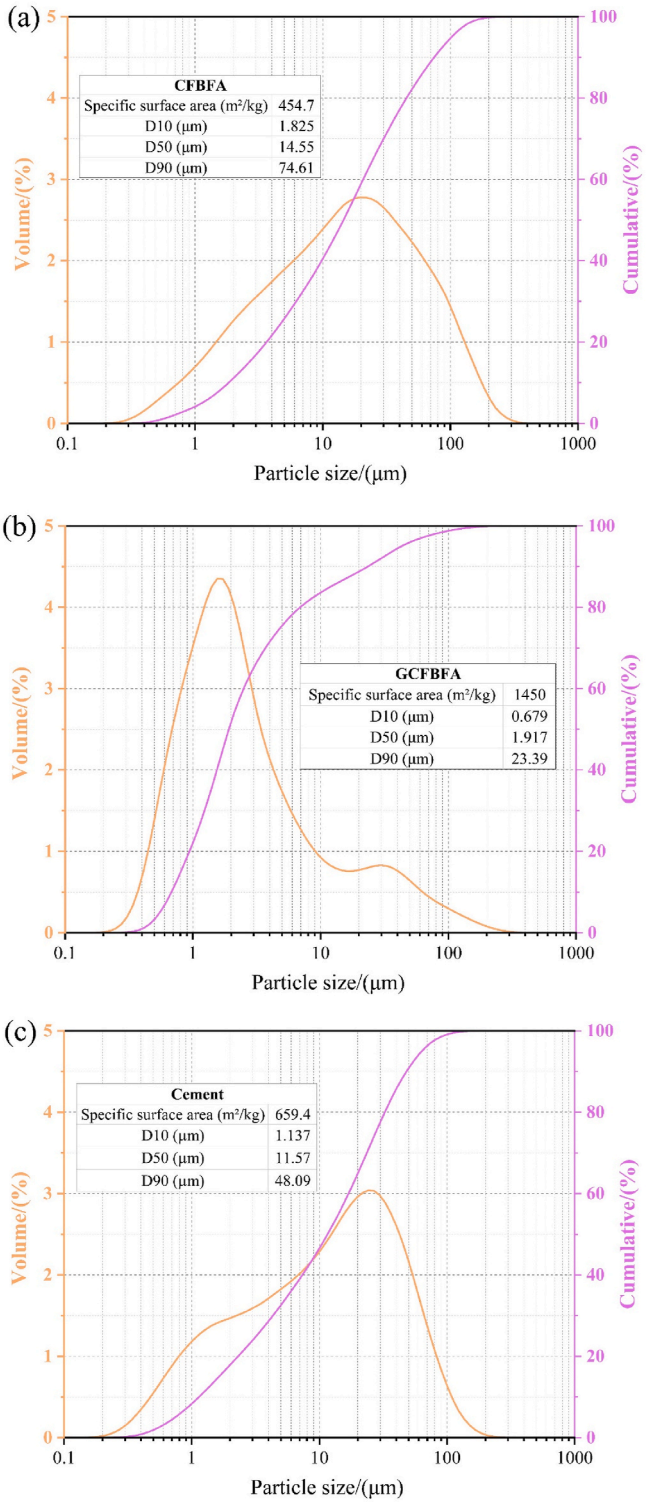

Fig. 2. Particle size distribution of CFBFA (a), GCFBFA (b), and cement (c).

2. Materials and methods

2.1. Materials

The constituent materials included P·I 42.5 Portland cement, CFBFA,

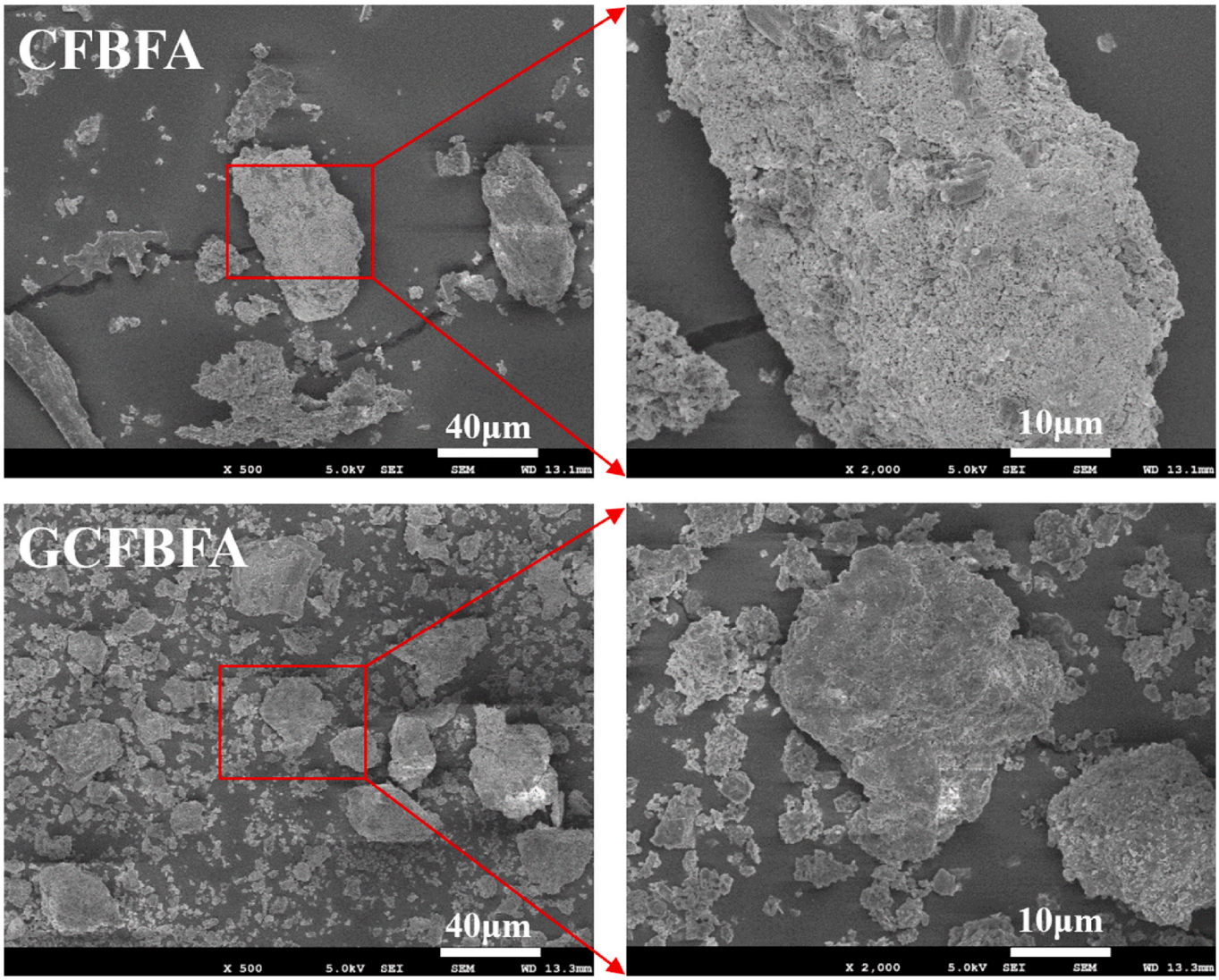

Fig. 3. The SEM images of CFBFA and GCFBFA.

and foaming agent. The apparent density of cement was 3110 kg/m^3. The CFBFA was produced in Shandong Province, China, with an apparent density of 2100 kg/m^3 and a loss on ignition of 15.89%. Table 1 shows the chemical composition of CFBFA and cement. The main components of CFBFA are SiO_2 and Al_2O_3. A small amount of Fe_2O_3, SO_3, CaO and TiO_2 appears as well. Fig. 1 presents the X-ray diffraction (XRD) pattern of CFBFA. The main mineral components of CFBFA are quartz (SiO_2), hematite (Fe_2O_3), anhydrite ($CaSO_4$) and vitreous components. It is worth noting that the alumina in CFBFA does not occur as mullite like that in ordinary fly ash, but rather as an amorphous vitreous form (He et al., 2021).

The GCFBFA was prepared by grinding CFBFA with a vibration mill for 4 min. Fig. 2 shows the particle size distribution. As it shows, the order of median particle diameters (D_{50}) from large to small is CFBFA (14.55 μm), cement (11.570 μm), and GCFBFA (1.917 μm). Compared with cement particles, the specific surface area of CFBFA is 31% smaller, while that of GCFBFA is 120% larger. Fig. 3 shows the Scanning electron microscopy (SEM) images of CFBFA and GCFBFA. It can be visualized that the CFBFA particles are large in size, irregular in shape, with small angular particles attached to the surface. After grinding, the particles become smaller, and the surface roughness is improved.

A composite polymer foaming agent was used, with a dilution ratio of 60 and a foaming ratio of 800–1000. The standard density of produced foam was 40–50 kg/m^3, with a 30 min bleeding rate of 15% and a 1-h settlement distance of 8.6 mm.

2.2. GCFBFA-cement binder

2.2.1. Setting time

The setting time test was conducted according to the Chinese standard GB/T 1346–2011. During the preparation of the standard consistency paste, the time when binder was added to the water was recorded as the onset of setting time. After preparation, the paste was placed in a standard curing environment. The first measurement was conducted 30 min after the onset time and every 5 min thereafter. For final setting time measurement, the interval was under 15 min.

2.2.2. Mechanical properties

The mechanical properties of GCFBFA-cement mortar were tested according to the Chinese standard GB/T 17671-2021. The binder/sand ratio was 1/3, with a w/b ratio of 0.5. The sand used was China ISO standard sand. Specimens are in size of 40 × 40 × 160 mm. The specimens were prepared and cured with molds in moisture at 20 °C for 24 h. Subsequently, the specimens were demolded and cured in water at 20 °C until test. Loading rates of compressive and flexural strength tests were 2.4 kN/s and 50 N/s, respectively. The flexural strength was the average of 3 specimens. And the compressive strength was averaged from 6 measurements.

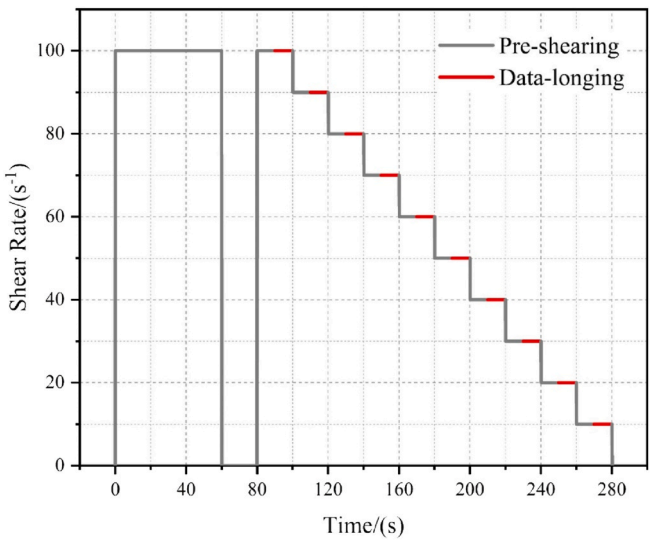

Fig. 4. A shearing schematic representation of the rheological test program.

2.2.3. Hydration products

XRD and Thermogravimetric Analysis (TGA) were applied for characterizing the hydration products of GCFBFA-cement blended paste. The 28 days cured specimen was broken into 2–3 mm fragments. The hydration was terminated by isopropanol exchange method (Zhang and Scherer, 2011). It was ground into powder after vacuum drying. For XRD test, the following parameters were set: CuKα target ray source, 40 kV voltage, 30 mA current, scanning speed of 1°/min, step size of 0.02°, and scanning angle of 5°–70°. For TGA, the temperature range was 20–800 °C, with a heating rate of 20 °C/min, and the atmosphere gas was nitrogen.

2.2.4. Hydration heat

The equipment used for hydration heat measurement was I-Cal 8000HPC 8-channel isothermal calorimeter. The cement and GCFBFA were weighed in proportion to a total of 30 g. The designed water-binder ratio was 0.5. After the cement-GCFBFA binder and water were mixed, the mix was immediately transferred into the calorimeter chamber to record the heat release continually up to 72 h for analysis.

2.2.5. Rheology

The rheological test referred to the standard ASTM C1749-17a. The AMETEK Brookfield RSX Soft Solids Tester Rheometer was used. The rotor used was CCT-40, and the sample chamber used was MBT-40. The test temperature was 20 °C. The same mixer and mixing program were used for all pastes. The rheological curve was measured 5 min after the fresh paste was prepared. This interval was used to prepare the rheology test and allow the fresh paste to reach a stable state for improving the repeatability of the data. Fig. 4 shows the rheological measurement program. The pre-shearing process with a shear speed of 100 s^{-1} for the first 60 s was adopted to ensure the uniform dispersion of paste (Wallevik et al., 2015). The shear rate was gradually decreased from 100 s^{-1} to 10 s^{-1}, with each step decreasing by 10 s^{-1}, and the holding time at each shear rate was 20 s (Zhou et al., 2022). For accurate and stable results, only the last 10 s data for each shear rate were used (Yuan et al., 2024). The Modified Bingham Model (1) was used to fit the curve and calculate the rheological parameters (Zhang et al., 2023a). It was described as:

$$\tau = \tau_0 + \mu\gamma + c\gamma^2 \quad (1)$$

Where: τ (Pa) is the shear stress, γ (s^{-1}) is the shear rate, τ_0 (Pa) is the yield stress, μ (Pa·s) is the plastic viscosity, c (Pa·s^2) is the second-order coefficient.

2.3. GCFBFA-cement LFC

2.3.1. Mixture proportions

To study the performance of LFC with different wet densities (600 kg/m^3, 700 kg/m^3, 800 kg/m^3) and GCFBFA substitution ratios (0%, 30%, 40%, 50%, 60%, 70%), 14 mixes were designed, as shown in Table 2.

2.3.2. Specimen preparation

As shown in Fig. 5, the pre-foaming method was employed to prepare GCFBFA-cement LFC, more details can be found in Ref. (Yuan et al., 2022). Cement-GCFBFA paste and foam were prepared separately. The foaming agent was mixed with water at a dilution ratio of 60. Following this, a foaming machine with a compressed air pressure of 0.4 MPa was used for the preparation of foam. Foam was then added to the mix within 1 min and stirred evenly. Before casting, measurements of the wet density and flowability were conducted. After that, the slurry was poured into the mold and sealed for 48 h at 20 °C. Before further tests, the specimens were demolded and preserved in a sealed bag under standard curing environment.

2.3.3. Fresh properties

The wet density was obtained by weighing the fresh LFC mix filled with a standard vessel, averaged from 3 measurements. Following the Chinese standard CJJ/T 177–2012, the flowability was tested through a mini-slump test. Firstly, the fresh mix was filled with a cylinder whose inner diameter and height were both 80 mm. The cylinder was then lifted vertically and slowly for the collapse of the mix. The maximum horizontal diameter of the slump was recorded after 1 min. The test was replicated 3 times. In order to evaluate the stability of fresh LFC slurry,

Table 2
Proportion of GCFBFA-cement LFC.

Mix	Targeted wet density (kg/m^3)	GCFBFA substitution ratio	W/b	GCFBFA (kg/m^3)	Cement (kg/m^3)	Water (kg/m^3)	Foam (kg/m^3)
D600S0	600	0%	0.5	0	377	188	36
D600S30		30%		113	264	189	36
D600S50		50%		189	189	189	35
D600S70		70%		265	113	189	34
D700S0	700	0%	0.5	0	446	223	27
D700S30		30%		134	312	223	28
D700S40		40%		179	268	223	30
D700S50		50%		223	223	223	30
D700S60		60%		268	179	223	32
D700S70		70%		313	134	223	33
D800S0	800	0%	0.5	0	514	258	25
D800S30		30%		154	360	258	24
D800S50		50%		258	258	258	24
D800S70		70%		361	155	258	22

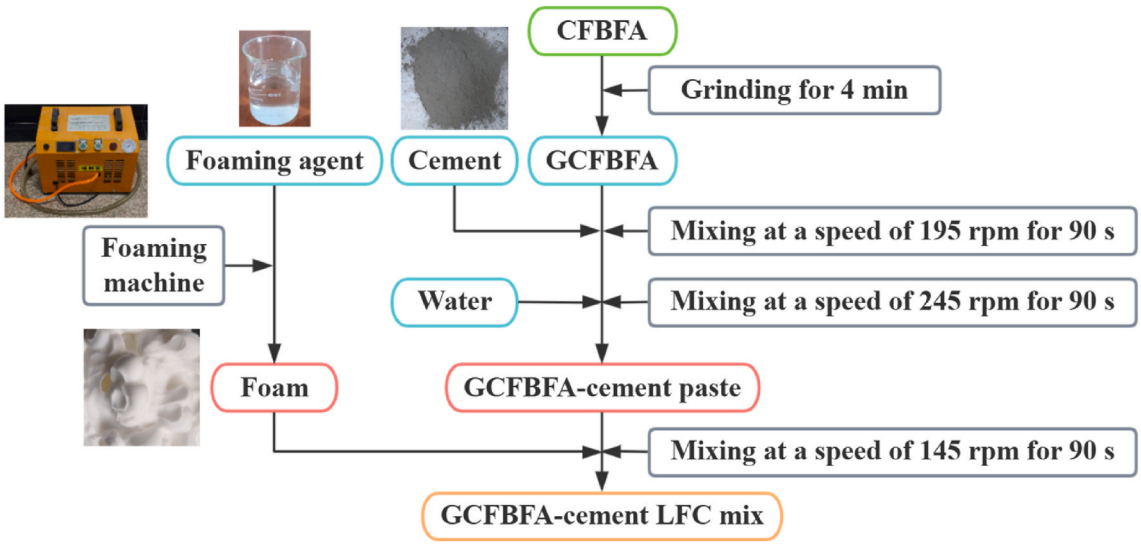

Fig. 5. Preparation process of GCFBFA-cement LFC.

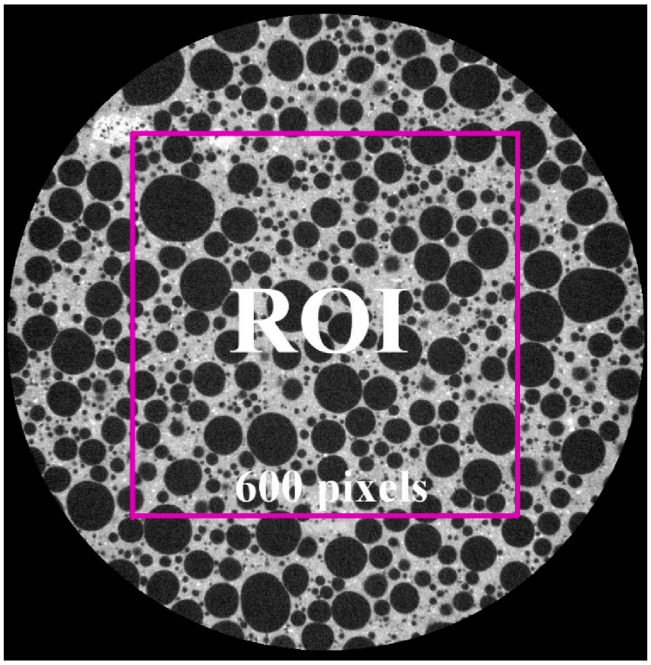

Fig. 6. One of the X-CT slices along the height of reconstructed LFC.

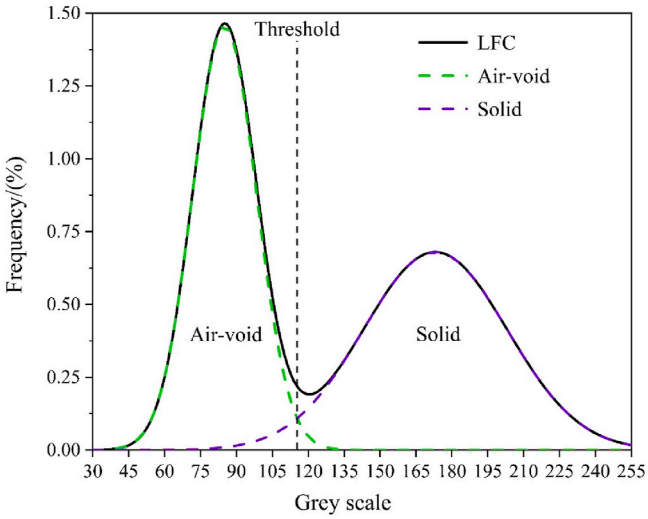

Fig. 7. The gray scale distribution curve of ROI.

the 1-h settlement was measured using a 50 ml cylinder and a laser displacement sensor.

2.3.4. Mechanical properties

The mechanical properties including compressive strength, splitting strength and elastic modulus were measured according to the standard GB/T 11969. 100 mm cubes were used for compressive and splitting strength tests. And the load rate was 1 mm/min 100 mm × 100 mm × 300 mm specimens were prepared for elastic modulus measurement. The mechanical properties reported are the average values of three specimens.

2.3.5. X-CT scanning and image segmentation

To obtain the air-void structure of LFC, 28 days cured cylindrical specimen (Φ50 mm × 130 mm) was scanned using the ZEISS Xradia 510 Versa 3D submicron imaging system. The X-CT scanning voltage was 110 kV, the current was 91 mA, the exposure time was 2 s, and the resolution was 25 μm.

After reconstruction, 1016 slices along height direction were extracted. A slice is shown in Fig. 6. Two phases, i.e., air-void (black) and solid matrix (gray) can be visualized. Square regions of interest (ROI), with a side length of 600 pixels were cut out from the center of slices. The color depth of the ROI images is then transformed from 16 bits to 8 bits, and the gray scale of each pixel was extracted for threshold determination. The gray scale distribution of ROI is shown in Fig. 7. The curve was deconvoluted into two Gaussian distributions. The intersection was considered to be the threshold between air-void and solid matrix. Pixels with grayscale value below the threshold represent air-voids, and vice versa represent the solid. Images before and after segmentation are compared in Fig. 8. A satisfactory result of threshold segmentation can be observed.

2.3.6. Water stability

LFC must be capable of resisting water damage when used for backfilling. Therefore, the evolution of water absorption and compressive strength of specimen under immersion were characterized. The specimens used were 100 mm cubes. The initial mass and compressive

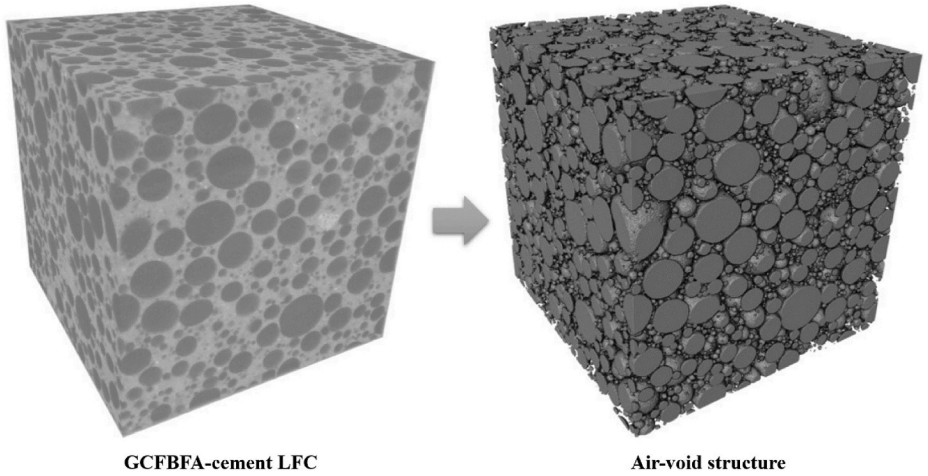

Fig. 8. The LFC image (left) before threshold segmentation and the air-void image (right) after threshold segmentation.

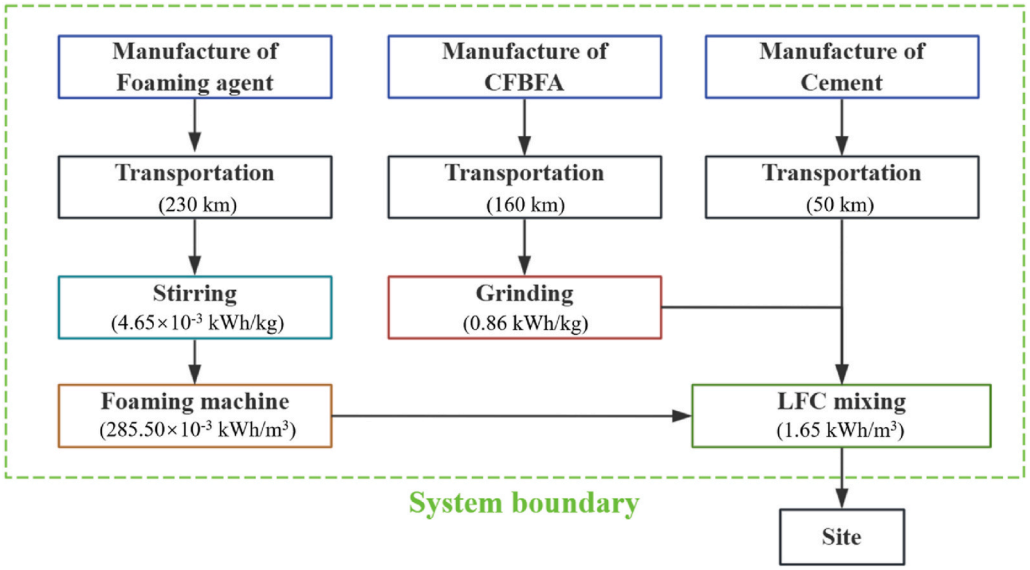

Fig. 9. System boundary for GCFBFA-cement LFC production.

strength were measured after curing for 28 days. Then specimens were immersed in water with temperature of 20 °C. The specimens were spaced at least 10 mm apart, with the upper and lower layers of specimens staggered and separated by metal mesh. The water surface was kept more than 30 mm above the upper surface of specimens. Before testing, the specimens were removed and the surface moisture was wiped off. Their mass and strength were measured after immersion for 7, 28, 56, 90 and 180 days, respectively. The measurement result was the average of 3 specimens.

2.3.7. *Freeze-thaw resistance*

Following GB/T 11969, the specimens prepared for test were 100 mm cubes. After curing for 28 days and soaking for 48 h, the specimens were in condition of saturated surface-dry (SSD). Then the mass was recorded. Afterwards, specimens were kept under freeze-thaw cycles (freezing at −20 °C for 6 h and thawing in water at 20 °C for 5 h). The distance from specimen to specimen and specimen to side was a minimum of 50 mm. The mass (SSD) and compressive strength (oven-dried) were measured after every 5 cycles. Three specimens were measured at a time and averaged. A total of 30 cycles were performed.

2.3.8. *Life cycle assessment*

The life cycle assessment (LCA) was conducted following the guidelines of ISO 14040 and ISO 14044. The modeling and analysis of LCA were performed using SimaPro 9.6 software. The system boundary of cradle-to-gate was shown in Fig. 9. The LCA considered the processes of the followings. The first process refers to the constituent phase, which encompassed the manufacture of raw materials of GCFBFA-cement LFC. The second is transportation phase, which involves the movement of materials from the manufacturing factory gates to site. In the end, it is the LFC production phase.

The inventory data were mainly obtained from the database Ecoinvent 3.10. Appropriate adjustments were made to the generic data based on the available local data. Trucks with a capacity of 10–20 metric tons were assumed for transportation. The global warming potential (GWP) and total cumulative energy demand were evaluated by ReCiPe 2016 Midpoint (H) and the Cumulative Energy Demand (Wagh and Gandhi, 2024).

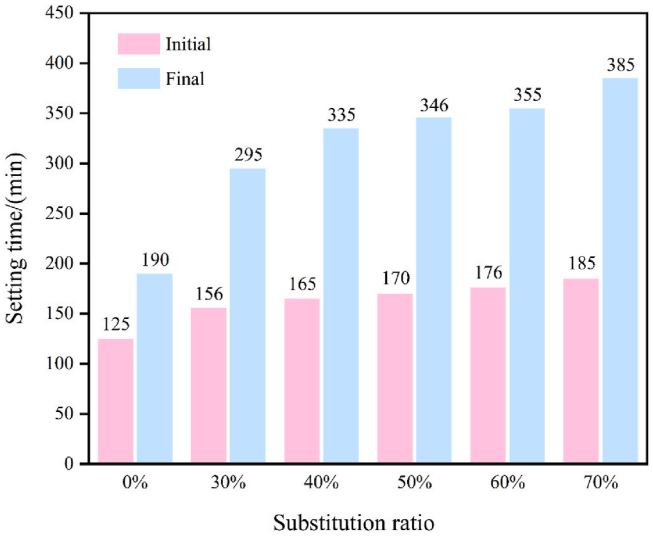

Fig. 10. Influence of GCFBFA substitution ratio on the setting time of cement.

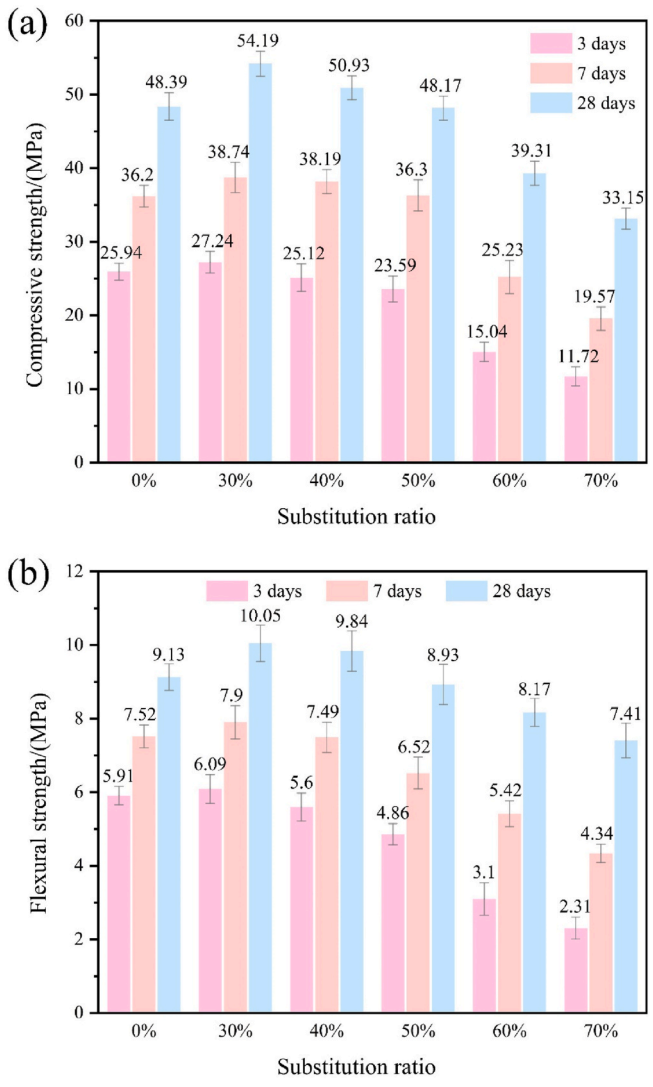

Fig. 11. Compressive strength (a) and flexural strength (b) of GCFBFA-cement mortar.

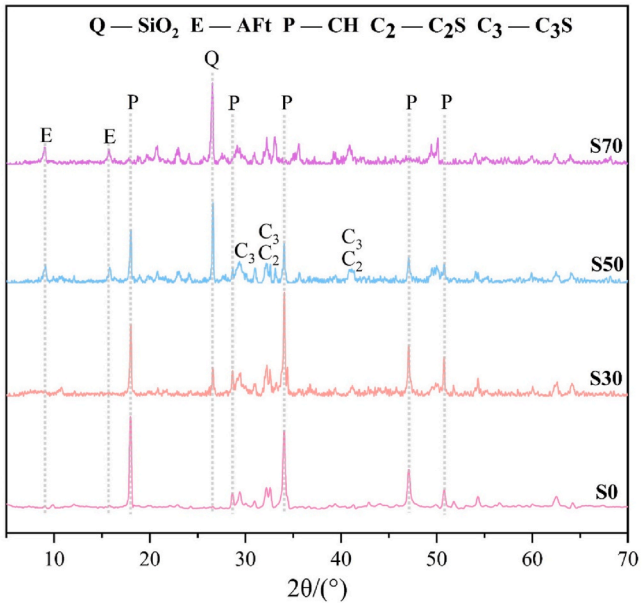

Fig. 12. Influence of GCFBFA substitution ratio on the XRD results at 28 days.

3. Results and discussion

3.1. GCFBFA-cement binders

3.1.1. Setting time

Fig. 10 shows the measured setting time of cement with different GCFBFA substitution ratios. As can be seen, GCFBFA causes the initial and final setting time of cement to be prolonged. The initial setting time of S30 and S70 is 156 min and 185 min, respectively, which is prolonged by 25% and 48% compared to S0. As for the final setting time, it is prolonged by 55% and 103% for S30 and S70, respectively. The above results show that the effect of GCFBFA on the final setting time is more significant. The prolonged setting time of GCFBFA-cement binder is beneficial for the transportation and construction.

3.1.2. Mechanical properties

Fig. 11 shows the effect of GCFBFA substitution ratio upon the compressive strength and flexural strength of GCFBFA-cement mortar. As shown in the figure, the mechanical strength of S30 is the highest. Compared with S0, the 28 days compressive and flexural strength of S30 are observed to be 12% and 10% higher, respectively. Also, a 5% and 3% increment in the 3 days compressive and flexural strength, respectively, is observed. It can be noticed that the contribution of GCFBFA to the later strength is more pronounced than that to the early strength. However, when GCFBFA exceeds the appropriate percentage, the strength shows a decreasing trend. Compared with S0, the 7 days compressive and flexural strength of S70 were found to be 46% and 42% lower, respectively. Additionally, the results of ultrafine circulating fluidized bed fly ash (UCFBFA) reported by ref (Zheng et al., 2023). are comparable to those herein. The incorporation of 30% UCFBFA brings improvement to the strength. Once UCFBFA dosage is above 30%, the strength decreases with UCFBFA content. Note that strengths of S50 are still on par with S0, confirming the utilization potential of GCFBFA.

3.1.3. Hydration products

The XRD patterns of GCFBFA-cement pastes were presented in Fig. 12. As it shows, the essential phases of the hardened pastes are CH (calcium hydroxide), SiO_2, AFt (ettringite) and unhydrated clinker minerals, including C_2S (dicalcium silicate) and C_3S (tricalcium silicate). The introduction of SiO_2 by GCFBFA leads to the enhancement of SiO_2 diffraction peak. As the GCFBFA substitution ratio increases, the

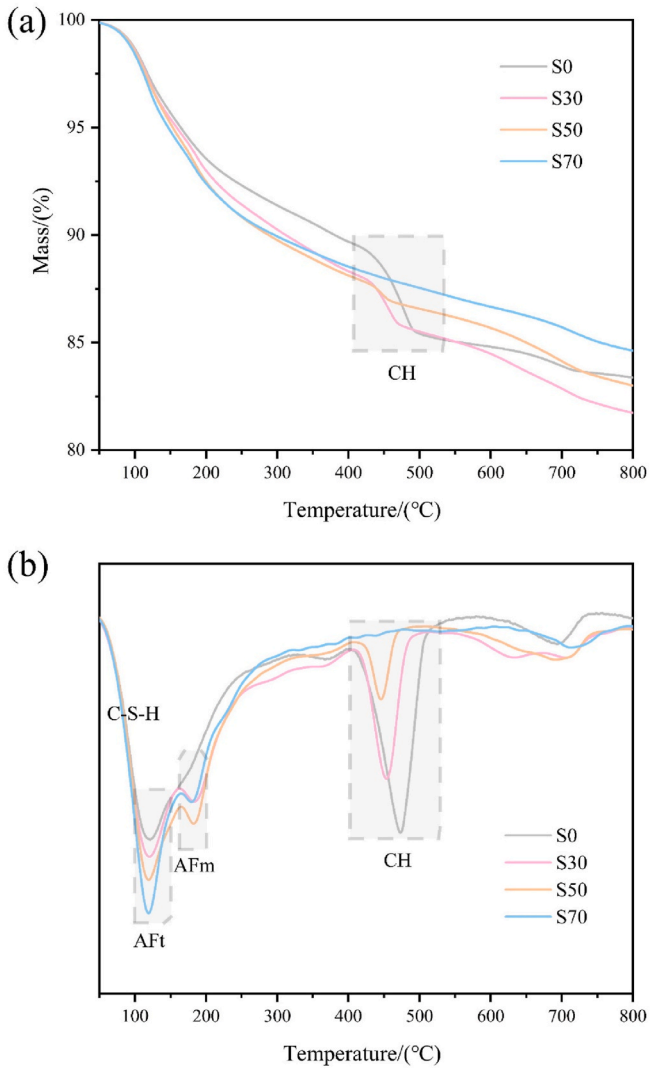

Fig. 13. Influence of GCFBFA substitution ratio on the TGA results at 28 days: (a) TG; (b) DTG.

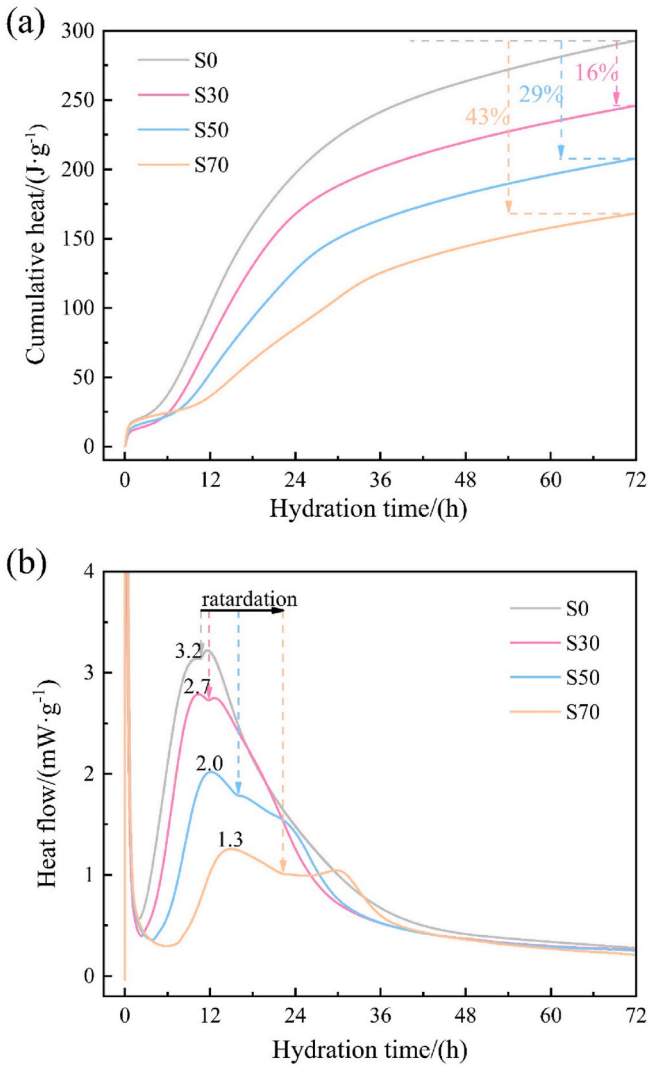

Fig. 14. Hydration results of GCFBFA-cement binder: (a) cumulative heat; (b) heat flow.

diffraction peak of CH at 18° gradually diminishes which disappears in S70. There are two reasons. One is the reduction of cement clinker. The second is the increase of GCFBFA possessing active SiO_2 and Al_2O_3 to set off pozzolanic reaction with CH. Because the core-shell structure of CaO in GCFBFA is destroyed by grinding, the CaO also hydrates to produce CH, and the diffraction peaks of CH at 34°, 47°, and 51° in S30 become stronger. A big difference in the XRD spectrums between S30 and S50 is found, while S30 has a smaller difference from S0. Compared with S30, the diffraction peak of SiO_2 in S50 increases remarkably, and that of CH decrease significantly. This indicates that the amount of CH is not sufficient to consume SiO_2 in S50. A comparative analysis of the results of S0, S30, and S50 reveals that the GCFBFA in S30 has a higher degree of reaction with cement. Additionally, an enhancement in the diffraction peaks associated with AFt is observed in S50 and S70, which can be attributed to the grinding-activated sulfate introduced by GCFBFA.

Fig. 13 shows the TGA results of the hardened GCFBFA-cement pastes at 28 days. As can be seen in Fig. 13a, after heating to 800 °C, the mass loss of S30 is the highest, S70 is the lowest, and S50 shows little difference with S0. This indicates that S30 has the most hydration products, and S70 has the least. As shown in Fig. 13b, in the range of room temperature to 300 °C, the C-S-H, AFt (100–150 °C) and monosulfoaluminate hydrate (AFm, 180–200 °C) are decomposed. CH and carbonates decompose in the intervals 350–550 °C and 650–750 °C, respectively. In the range of 350–550 °C, with increase of GCFBFA substitution ratio, the mass loss gradually decreases, and the thermal decomposition peak area of CH decreases significantly. This means the total amount of CH decreases with the GCFBFA substitution ratio. The cementitious material of S70 contains 30% cement, but the thermal decomposition peak of CH in S70 disappears, indicating the consumption of CH by GCFBFA. This finding is in alignment with the XRD results. Furthermore, because of the sulfate introduced by GCFBFA, the thermal decomposition peak area of AFt increases with GCFBFA substitution ratio. For the same reason, the thermal decomposition peak area of AFm increases with GCFBFA substitution ratio until 50%. S70 has less AFm than S50. This can be explained by the inhibition of the conversion of AFt to AFm by adequate sulfate and the decrease of C_3A from cement clinker.

3.1.4. Hydration heat

Fig. 14a shows the effect of GCFBFA substitution on the cumulative heat release. As it presents, the cumulative heat release decreases significantly with GCFBFA substitution ratio. Compared with S0, the cumulative heat release of S30, S50, and S70 decrease by 16%, 29%, and 43%, respectively. The reduction in exothermic heat helps in reducing the thermal stress and the associated cracking, which is favorable for massive construction (Wang et al., 2018a).

Table 3
The heat release per gram of cement (excluding GCFBFA) at 72 h.

Mix	S0	S30	S50	S70
Heat release per gram of cement (J/g cement)	293	351	415	560

Note: the heat release per gram of cement is calculated as the cumulative heat release divided by the mass of cement, which excludes the mass of GCFBFA.

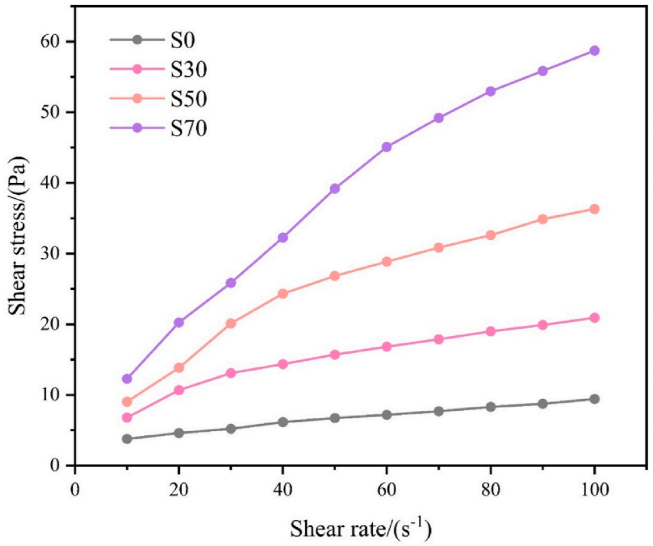

Fig. 15. Effect of GCFBFA substitution ratio on the rheological curve.

The heat release per gram of cement (excluding GCFBFA) at 72 h is shown in Table 3. As it shows, the heat release per gram of cement increases with GCFBFA substitution ratio. Compared with S0, the heat release per gram of cement in S30, S50, and S70 increase by 20%, 42%, and 91%, respectively. It is owing to that GCFBFA provides activated SiO_2 and Al_2O_3 which react with the CH from cement hydration. Besides, the GCFBFA particle not only provides nucleation site, plays a seed effect, but also increases the effective water-cement ratio, improving the hydration degree of cement (Zhao et al., 2018).

Fig. 14b shows the influence of GCFBFA substitution ratio upon the heat release rate. The results of GCFBFA-cement binders are comparable to the result of pure cement binder. It demonstrates that GCFBFA doesn't change the main process of hydration, corresponding to 5 periods: initial, induction, acceleration, deceleration, and stable period (John and Lothenbach, 2023). During the initial period, the C_3A in cement and aluminum phase in GCFBFA react with sulfate producing AFt. In this period, the heat is released intensely. Afterwards, the concentration of Ca^{2+} gradually increases in the induction period.

As can be seen in Fig. 14b, GCFBFA extends the duration of the induction period. And the prolongation effect is enhanced with the increase of GCFBFA substitution ratio. This explains that the incorporation of GCFBFA leads to a prolonged setting time. There are 2 reasons for the extension of the induction period. Firstly, GCFBFA dilutes the cement, leading to a lower concentration of Ca^{2+}. Also, the reduction of cement results in less actual hydrating material. Secondly, the AFt generated by the reaction of aluminum phase with sulfate introduced by GCFBFA delays hydration (Mbasha et al., 2020). In the acceleration period, C_3S and C_2S are further hydrated, the heat release rate increases, and a second exothermic peak occurs. The peak exothermic rates of S30, S50, and S70 is 16%, 38%, and 59% lower than S0, respectively. With increase of GCFBFA substitution ratio, the rise of the second exothermic peak slows down and the peak exothermic rate decreases, owing to the dilution of cement by GCFBFA. Furthermore, as the substitution ratio increases, the appearance of the third peak is retarded, the peak exothermic rate decreases, and the peak gradually becomes wider. It's attributed to the sulfate introduced by GCFBFA, which delays the reaction between C_3A and AFt to produce AFm (Sun et al., 2022).

Table 4
The rheological parameters of GCFBFA-cement binders.

Mix	Yield stress τ_0 (Pa)	Plastic viscosity μ (Pa·s)	Second-order coefficient c (Pa·s^2)
S0	3.054	0.081	−0.00018
S30	5.159	0.271	−0.00118
S50	3.921	0.587	−0.00271
S70	3.666	0.864	−0.00312

3.1.5. Rheology

Fig. 15 shows the measured rheological curves of GCFBFA-cement paste blends. At an identical shear rate, the shear stress demonstrates an increase with the substitution ratio. The rheological curve of S0 is approximately linear, indicating a similarity between the fresh neat cement paste and Bingham fluid. The paste blends begin to show features of a non-Newtonian fluid with increase of the GCFBFA substitution ratio. The phenomenon of shear thinning becomes increasingly apparent. This illustrates the promoting effect of GCFBFA on the flocculation of paste (Zhang et al., 2022a; Wang et al., 2021).

Table 4 shows the calculated rheological parameters. It is obvious that the plastic viscosity increases with GCFBFA substitution ratio. Compared with S0, the plastic viscosity of S30, S50 and S70 increase by 235%, 625%, and 967%, respectively. This can be attributed to the fact discussed above in which the fine GCFBFA particles tend to agglomerate and form a flocculated mesh structure in the slurry (Han et al., 2022). It can be rationalized as charge attraction and particle aggregation (Liu et al., 2024). The silicon and aluminum on the GCFBFA particle surface absorb OH^- when in contact with water. They become negatively charged, and attract the CH micelles which are positively charged to form agglomerated particles, causing an increase in the plastic viscosity and yield stress (Xia et al., 2013).

As shown in Table 4, yield stress of S30 is by 69% higher compared to S0. One reason is the enhanced flocculation (Xiong et al., 2024). Another reason is that the GCFBFA particles increase the specific surface area of the blend, thereby reducing the water film thickness and increasing the inter-particle friction resistance. However, the yield stress decreases when the GCFBFA substitution ratio exceeds 30%. Compared with S30, the yield stress of S50 and S70 decrease by 24% and 29%, respectively. This is attributable to the shape effect and size effect of GCFBFA particles (Zhang et al., 2022b). When the substitution ratio is relatively high, the fine GCFBFA particles provide lubrication and weaken the compacting of large particles (Zheng et al., 2017). Nevertheless, the GCFBFA-cement binders have increased rheological properties, including the plastic viscosity and yield stress, compared to the pure cement binder.

3.2. GCFBFA-cement LFC

3.2.1. Fresh properties

Table 5 presents the measured fresh properties of LFC. In view of wet density, there is a discrepancy of less than 2% between the targeted and actual values. This means that there was no segregation or bleeding throughout the preparation of specimens. The incorporation of foam has a deleterious impact on the flow of slurry, thus the flowability increases with wet density. With increase of GCFBFA substitution ratio, the flowability decreases. This can be ascribed to the increase of plastic viscosity. Nevertheless, the flowability of mixes were between 160 mm and 190 mm, satisfying the requirement for cast-in-place LFC.

As shown in Table 5, the stability of fresh LFC slurry increases with wet density. The 1-h settlements of D600S50, D700S50, and D800S50 are 2.193 mm, 1.936 mm, and 1.598 mm, respectively. This is related to the foam content. With increase of GCFBFA substitution ratio, the stability of fresh LFC slurry improves first and declines when the

Table 5
Fresh properties of GCFBFA-cement LFC.

Mix	Targeted wet density (kg/m^3)	GCFBFA substitution ratio	Actual wet density (kg/m^3)	Density ratio	Flowability (mm)	1-h settlement (mm)
D600S0	600	0%	595	0.992	183	2.349
D600S30		30%	603	1.005	180	1.785
D600S50		50%	610	1.017	172	2.193
D600S70		70%	589	0.982	161	2.534
D700S0	700	0%	701	1.001	185	2.082
D700S30		30%	711	1.016	183	1.573
D700S40		40%	695	0.993	179	1.759
D700S50		50%	696	0.994	175	1.936
D700S60		60%	698	0.997	168	2.085
D700S70		70%	703	1.004	163	2.238
D800S0	800	0%	802	1.003	188	1.702
D800S30		30%	797	0.996	185	1.303
D800S50		50%	792	0.990	178	1.598
D800S70		70%	799	0.999	166	1.841

substitution ratio exceeds 50%. The 1-h settlements of D700S0, D700S30, and D700S70 are 2.082 mm, 1.573 mm, and 2.283 mm, respectively. The improved stability of fresh LFC slurry can be attributed to the increased yield stress and plastic viscosity. When the GCFBFA substitution ratio exceeds 50%, the reduction in the yield stress, cement content, and hydration rate result in a decline in the stability of fresh LFC slurry (Raj et al., 2019). Tran et al. (2022) reported that the yield stress, plastic viscosity, setting time, and consistency of fresh LFC slurry contribute significantly to the stability of bubbles, affecting the hardened properties such as mechanical strength, elastic modulus and durability.

3.2.2. Mechanical properties

Fig. 16 shows the effect of wet density and GCFBFA substitution ratio on the compressive strength (f_c). It is evident that f_c increases with wet density. Compared with D600S50, the 28 days f_c of D700S50 and D800S50 increases by 40% and 108%, respectively. This is anticipated, as the higher density generally corresponds to a higher f_c because of the reduced air-void volume (Othman et al., 2021).

The incorporation of 30% GCFBFA was observed to enhance the f_c of LFC. The 28 days f_c of D700S0 is 1.80 MPa, while that of D700S30 is 2.04 MPa, increasing by 13%. There are 2 main reasons for the strength increment. On one side, as mentioned before, the hydration degree of cement was promoted by GCFBFA, generating more hydration products, together with the filling effect (Thiyagarajan et al., 2022) of GCFBFA particles, the matrix of LFC is strengthened. Another reason may be derived from the optimization of air-void structure, discussed in the following section. However, when the GCFBFA substitution ratio exceeds 30%, the f_c shows a decreasing trend because of the decrease in cement content. The 28 days f_c of D700S50 and D700S70 is 1.58 MPa and 1.19 MPa, respectively, which is 12% and 34% lower than D700S0. Nevertheless, the 28 days f_c of D600S70, the lowest f_c of all mix proportions, meets the requirement (0.8 MPa) of subgrade filling (JTG D30-2015).

Table 6 lists the measured splitting tensile strength (f_{ts}) and elastic modulus (E_c) of GCFBFA-cement LFC. They follow the same trend with wet density and GCFBFA substitution ratio as f_c. The mechanical properties increase with wet density. Compared with D600S50, the 28 days f_{ts} of D700S50 and D800S50 is higher by 33% and 67%, respectively. Compared to f_c, the increase ratio in f_{ts} with wet density is lower. Compared with D600S50, the E_c of D700S50 and D800S50 shows an increase of 74% and 144%, respectively. This increment is more pronounced than the one observed in f_c. Besides, incorporation of 30% GCFBFA increases the 28 days f_{ts} and E_c by 17% and 20%, respectively. Both increments are higher than that in f_c.

Fig. 17 illustrates the relation between f_{ts} and f_c. The determination coefficient is 0.94. The f_{ts} increases with f_c, meeting the relationship: $f_{ts} = 0.18 f_c^{0.81}$. Thus, in practical applications, it is possible to make a prediction of f_{ts} based on f_c. The ratio of f_{ts} to f_c for GCFBFA-cement LFC varies between 0.15 and 0.21, representing a higher value than that reported for concrete containing aggregates (0.07–0.15) (Ge et al., 2020; Raj et al., 2019). This is one of the benefits of aggregate absence, as it reduces the interfacial transition zone that is detrimental to the tensile strength (Awoyera and Britto, 2020).

The correlation between the 28 days E_c and f_c is shown in Fig. 18. The determination coefficient is 0.95, indicating a significant positive correlation which can be expressed as: $E_c = 0.75 f_c^{1.19}$. The main reason for the low elastic modulus of LFC is the porous structure which leads to a low density. Ref (Raj et al., 2019). reported that E_c of LFC is reduced in comparison to normal concrete because of the absence of aggregate. Nonetheless, the E_c to f_c ratio is 0.7–0.95, which is in the range of normal concrete (0.3–1.2) (Vu et al., 2021). Furthermore, the E_c of the studied GCFBFA-cement LFC is sufficient to satisfy the requirement (70 MPa) for subgrade filling (Ge et al., 2020).

3.2.3. Air-void structure

The performance of LFC depends on more than just the matrix. Unlike other concretes, LFC is distinguished by the presence of a significant volume of air-voids. Larger volume of air-voids brings it light weight, thermal insulation, higher strength ratio, economic effectiveness and other advantages. But the air-voids usually act as stress concentration sites and weak spot where failure initiates (Narayanan and Ramamurthy, 2000). It is essential for LFC to optimize the air-void structure, specifically the volume, size, and shape, in order to achieve the desired properties (Zhou et al., 2021; Falliano et al., 2019).

The segmented air-void structure in a cubic space with length of 15 mm is shown in Fig. 19. As it shows, the air-voids are spherical and are either interconnected or enclosed. To prepare LFC, the incorporation of the blended foam into the slurry results in the formation of numerous minute air-voids with a diameter of less than 200 μm. Although they are small, they make up most of the air-void structure. The remaining large air-voids are formed by the merging of small ones during the formation of LFC structure. The characteristic parameters (air-void volume, equivalent diameter and sphericity) are used for characterizing the structure. Air-void volume is the sum of all the air phase, which is the most influential among all the parameters (Nambiar and Ramamurthy, 2007). The equivalent air-void diameter and sphericity are calculated following the method proposed in paper (Jiang et al., 2022).

The effect of wet density on the characteristic parameters is listed in Table 7. The air-void volume of D700S50 and D800S50 decreases by 7.1% and 13.7%, respectively, compared to D600S50. This can be explained by the lower foam content in the higher density mix. In accordance with Ostwald's theory, small bubbles are swallowed by large bubbles forming larger ones, driven by the interfacial free energy. (Song et al., 2021). The decrease in foam decreases the probability of air-void merging and overlapping (Zhu et al., 2024), which prevents the air-void

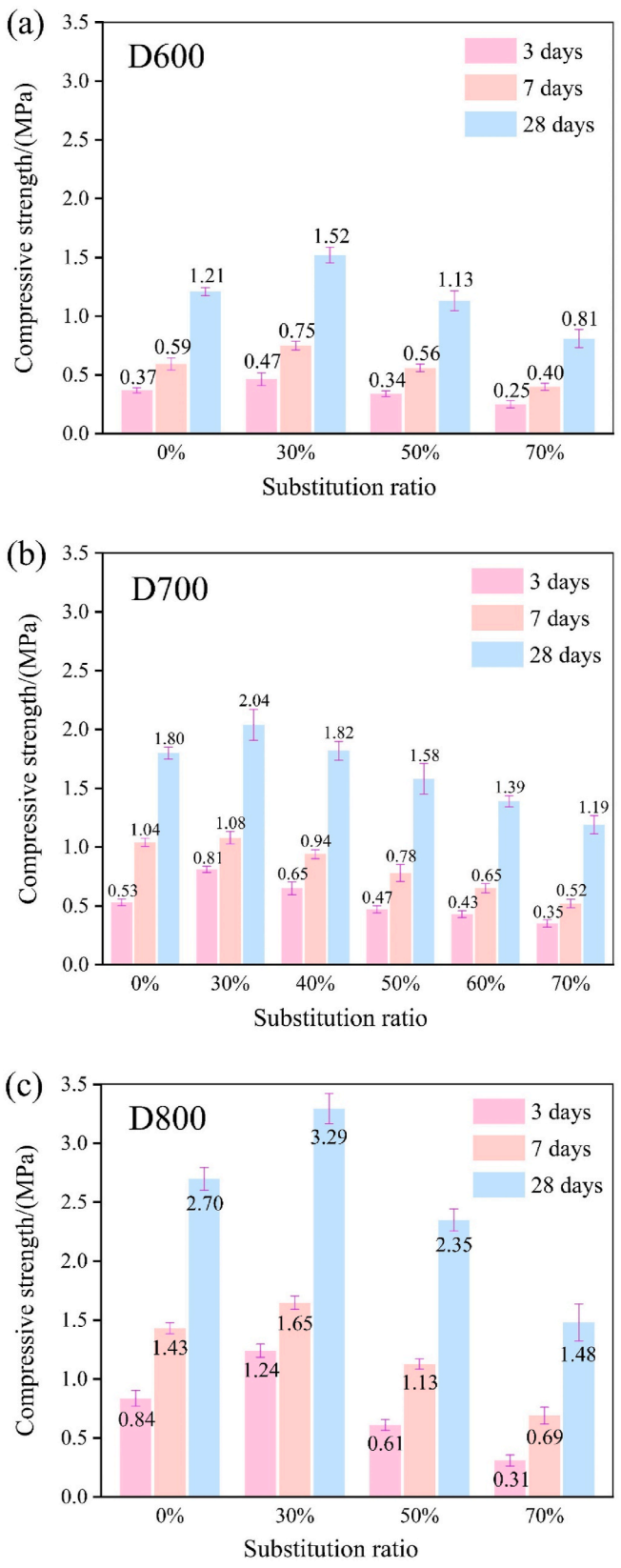

Fig. 16. Compressive strength of GCFBFA-cement LFC with different wet densities: (a) D600; (b) D700; (C) D800.

Table 6
Splitting strength (f_{ts}) and elastic modulus (E_c) of LFC.

Code	7 days f_{ts} (MPa)	28 days f_{ts} (MPa)	28 days E_c (GPa)
D700S0	0.17	0.29	1.55
D700S30	0.22	0.34	1.86
D700S50	0.15	0.28	1.39
D700S70	0.08	0.21	0.84
D600S50	0.10	0.21	0.80
D800S50	0.24	0.35	1.95

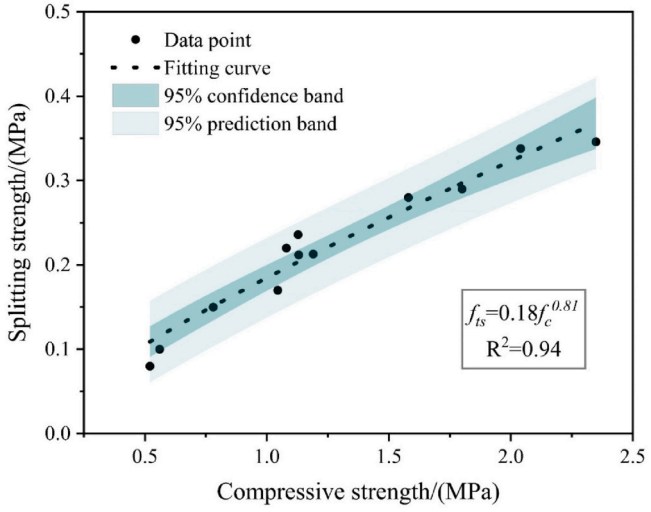

Fig. 17. Relationship between the splitting strength and compressive strength.

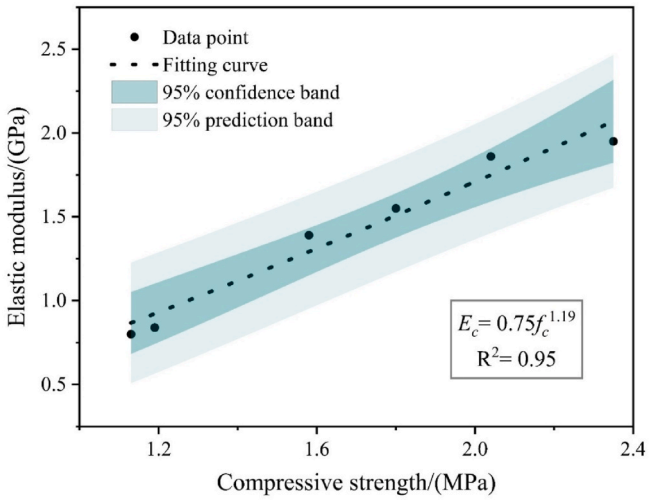

Fig. 18. Relationship between the elastic modulus and compressive strength at 28 days.

from becoming large and irregular. As a result, compared with D600S50, the equivalent diameter of D700S50 and D800S50 decreases by 11.2% and 21.7%, respectively. And the sphericity increases by 4.8% and 10.8%, respectively. Similar observation was reported in ref (Hilal et al., 2015). that density dominates the air-void properties, and the volume play a more important role than the size and shape.

The influence of GCFBFA on the characteristic parameters is illustrated in Table 7. Compared with D700S0, the air-void volume and equivalent diameter of D700S30 decrease, as well as the sphericity improves. The optimized air-void structure of D700S30 comes from three sides. Firstly, the fine GCFBFA particles fill part of air-voids through

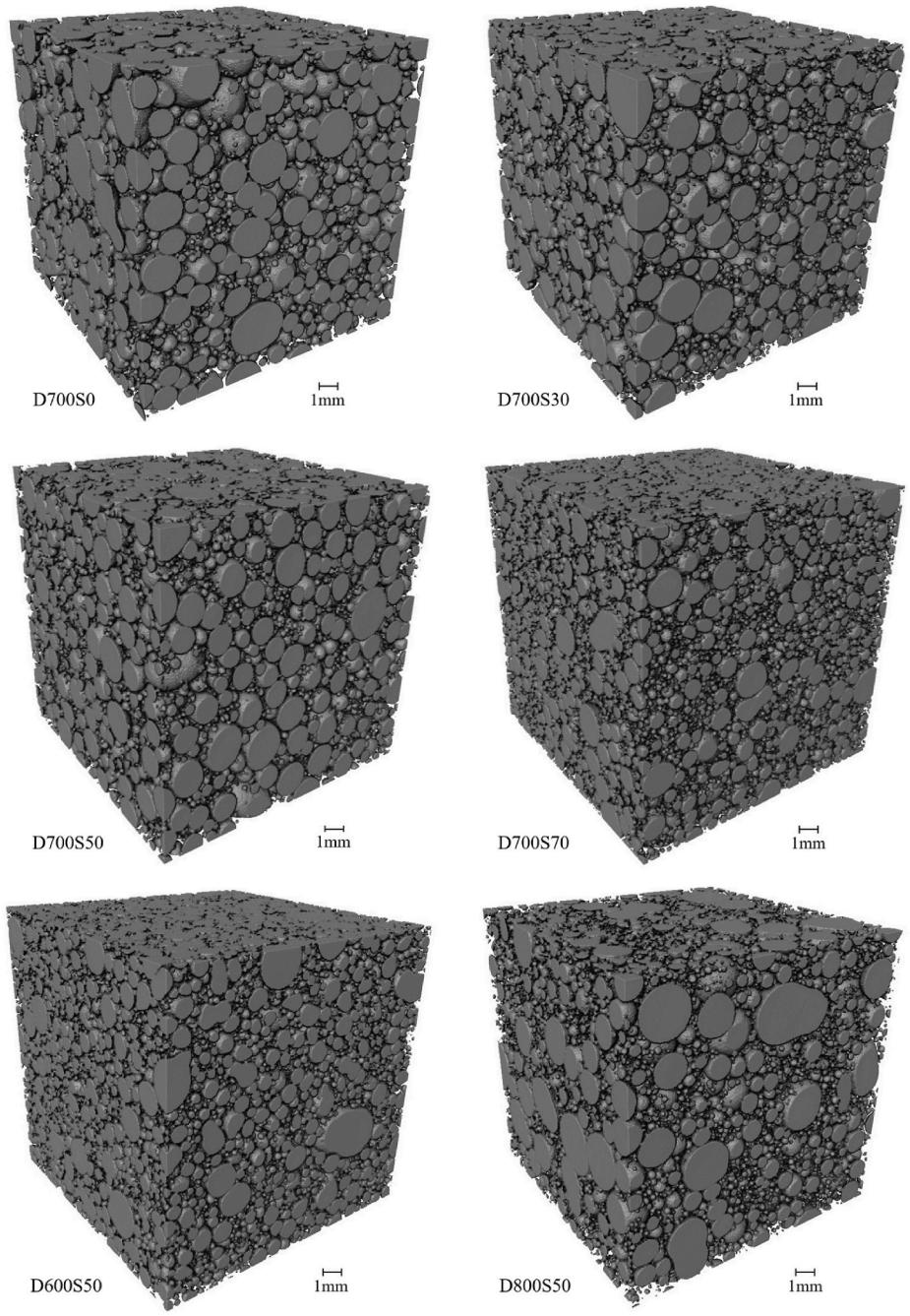

Fig. 19. Three-dimensional air-void structure of LFC.

Table 7
Measured air-void structure characteristic parameters of LFC.

Parameters	D600S50	D700S0	D700S30	D700S50	D700S70	D800S50
Volume (%)	59.5	50.9	46.7	52.4	57.3	45.8
Equivalent diameter (μm)	145.5	126.6	121.7	129.2	139.1	113.9
Sphericity	0.83	0.88	0.90	0.87	0.85	0.92

Note: the closer the sphericity is to 1, the closer the shape of the air-void is to a sphere.

micro-aggregate effect (Yang et al., 2020). Secondly, the plastic viscosity and yield stress of slurry with addition of 30% GCFBFA becomes higher, which improves the binding force on the foam and restrains the foam from migrating and merging, resulting in a more stable foam (Jiang et al., 2024; Wang et al., 2018b). Thirdly, the fine pozzolanic particles can inhibit the deterioration of foam during the hardening process (Hou et al., 2019; Qi et al., 2024).

Compared with D700S0, the air-void volume of D700S70 increases by 6.4%. This is mainly because, as cement decreases, the amount of hydration products decreases, leading to the poor filling of air-voids. Furthermore, the equivalent diameter of D700S70 increases by 9.9%, and the sphericity decreases by 3.4%. This is because the inhibition of

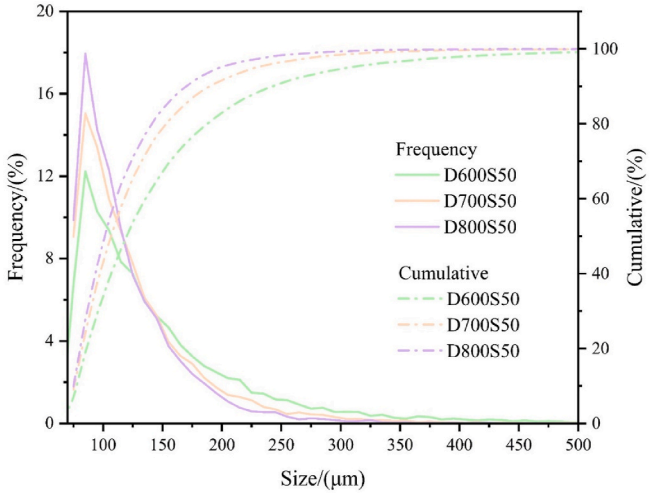

Fig. 20. Effect of wet density on the air-void size distribution.

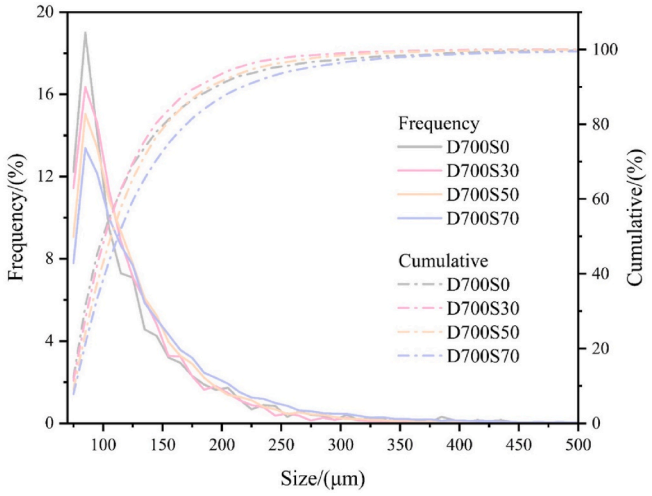

Fig. 21. Effect of GCFBFA substitution ratio on the air-void size distribution.

foam deterioration by the mixture diminishes along with the decrease in the yield stress. Another reason is that GCFBFA slows down the hydration reaction, leading to slower hardening of the matrix. Air-void merging and overlapping occurs during the extended hardening period (Hou et al., 2019).

Figs. 20 and 21 show the effect of wet density and GCFBFA substitution on the air-void size distribution, respectively. As illustrated, there is an observable increase and subsequent decrease in the frequency with air-void size. The size of air-void with the highest frequency is about 85 μm. The proportion of air-voids with size below 200 μm is above 80%. The large air-voids are prone to stress concentrations under load, which is detrimental to the performance (Nambiar and Ramamurthy, 2007). As illustrated in Fig. 20, with increase of wet density, the amount of small air-voids (size below 100 μm) increases and the amount of large air-voids (size above 200 μm) decreases. As discussed above, this is mainly an effect of foam content, and similar result is reported by Yao et al. (2023b). As illustrated in Fig. 21, compared with D700S0, the frequency of air-voids with size above 200 μm decreases in D700S30, and increases in D700S70. This illustrates that the proper incorporation of GCFBFA reduces the proportion of large air-void in LFC.

Relationships between the characteristic parameters and the 28 days compressive strength are shown in Fig. 22. As illustrated, the strength increases with decrease of air-void volume, equivalent diameter, and increase of sphericity, respectively. The determination coefficients of

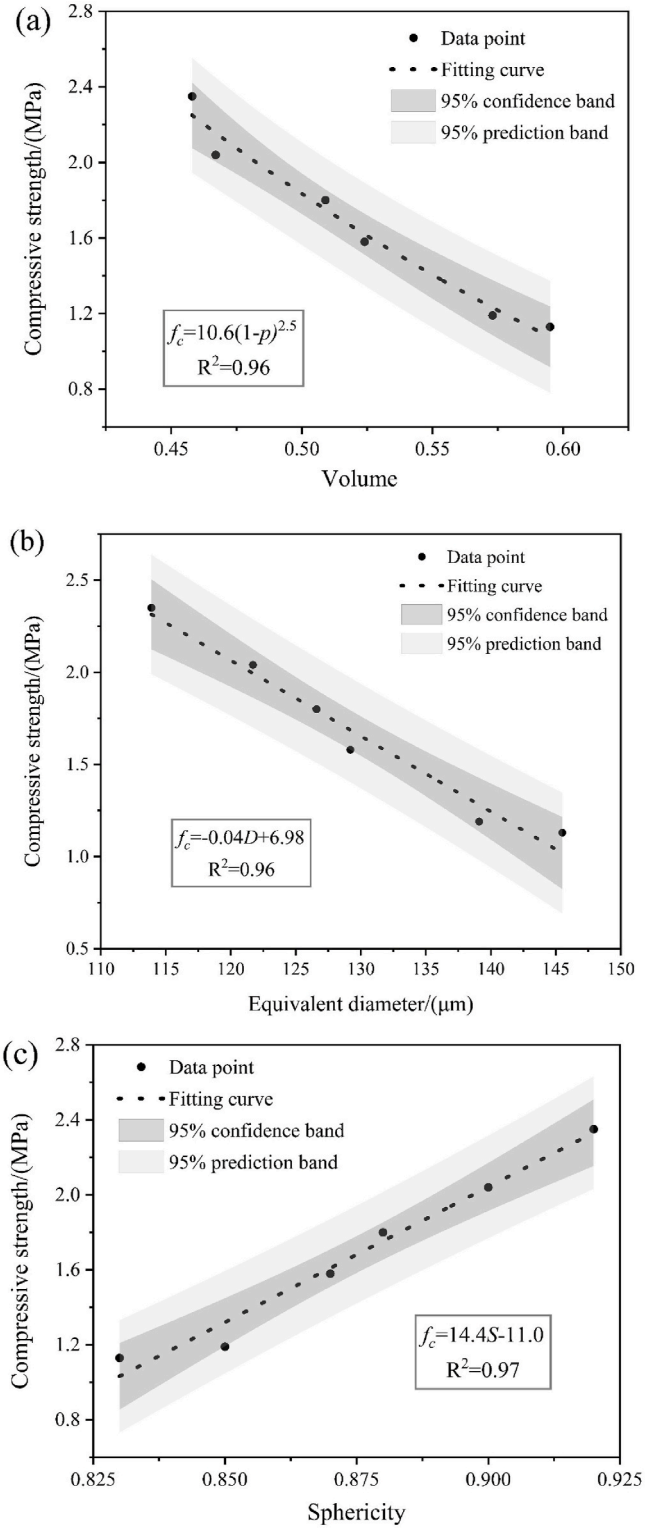

Fig. 22. Relationship between the air-void structure parameters and the 28 days compressive strength: (a) volume; (b) equivalent diameter; (c) sphericity.

fittings are above 0.96, verifying the important role that air-void structure plays in the strength of LFC.

3.2.4. *Water stability*

Effect of wet density on the water absorption is shown in Fig. 23a. As illustrated, the water absorption increases with soaking time, and it gradually becomes stable. The water absorption decreases with wet

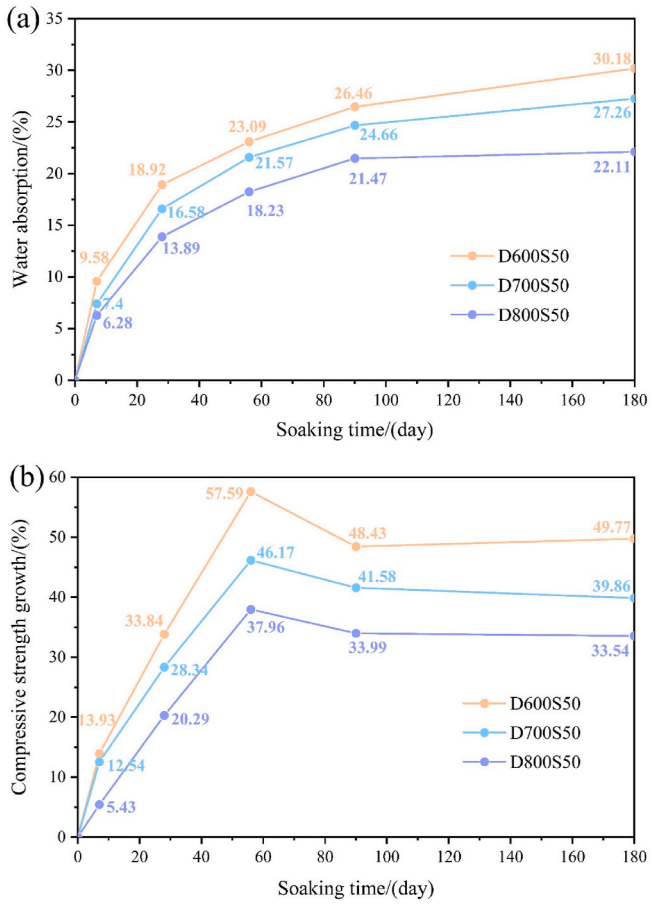

Fig. 23. Effect of wet density on the water absorption (a) and compressive strength (b) of LFC after soaking.

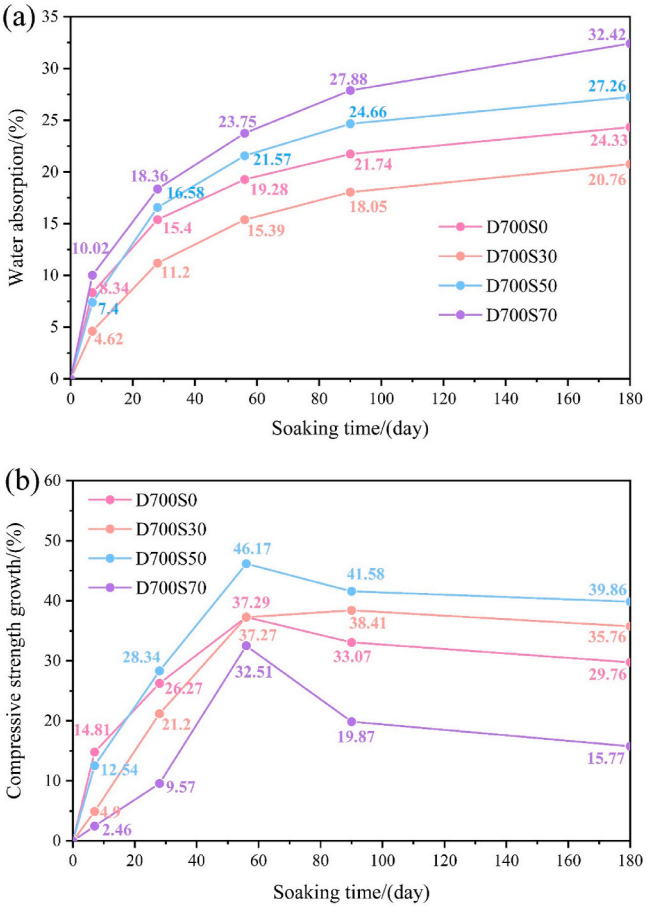

Fig. 24. Effect of GCFBFA substitution ratio on the water absorption (a) and compressive strength (b) of LFC after soaking.

density. The 180 days water absorption of D800S50 is 22.11% which is lower by 8.07% compared with D600S50. The air-voids are passages for moisture to enter, so LFC with higher density typically exhibits lower water absorption owing to its lower air-void volume (Makul and Sua-iam, 2016).

Fig. 23b shows the effect of wet density on the compressive strength. The strength gradually increases during the first 56 days of soaking. After soaking for 56 days, the strength of each mix increases by more than 35%. This is because the cement and GCFBFA continues hydrating, especially in the presence of sufficient moisture. The strength increment decreases with wet density. This is due to the lower water absorption of higher density LFC. However, strength shows a decrease after 90 days of soaking. From 56 to 90 days of soaking, the strength growth ratio of D600S50, D700S50 and D800S50 decreases by 9.16%, 4.59% and 3.97%, respectively. This is also related to the water absorption. Excessive soaking has a softening effect on LFC, thus impairing its strength (Wang et al., 2019). It is noticeable that the strength stabilizes after 90 days of soaking.

Fig. 24a shows the effect of GCFBFA substitution ratio on the water absorption. The water absorption first decreases and then followed by an increase with GCFBFA substitution ratio. The water absorption ratio of D700S30 is the lowest, which is 20.76% at 180 days of soaking, achieving a 3.57% reduction compared to D700S0. This is because the incorporation of 30% GCFBFA reduces the air-void volume by 4.2%. On the contrary, compared with D700S0, the water absorption ratio of D700S50 and D700S70 increases by 2.93% and 8.09%, respectively. The incorporation of more GCFBFA increases the water absorption because of the increase in interconnected air-void volume (Li et al., 2021c).

Fig. 24b shows the effect of GCFBFA substitution ratio on the strength. Compared with D700S0, the strength growth ratio of D700S30 and D700S50 increase, and that of D700S70 decreases. After 56 days of soaking, the strength growth ratio of D700S50 is the highest, increasing by 46.17%. One reason is the high water absorption of D700S50 caused by the high air-void volume. For another reason, the incompletely reacted SiO_2 in D700S50 continues to react with CH under sufficient moisture condition. The compressive strength growth ratio of D700S70 is the lowest, increasing by 32.51%. This is a result of cement reduction owing to the substitution. During the 56–180 days of soaking, the strength loss of D700S0, D700S30, D700S50 and D700S70 is 7.53%, 1.51%, 6.31% and 16.74%, respectively. Because of the high water absorption ratio and the low matrix strength caused by low cement content, the compressive loss of D700S70 is the highest. However, the compressive strength of D700S70 after 180 days of soaking (D700S70) still increases by more than 15%. This demonstrates the satisfactory strength property of GCFBFA-cement LFC in submerged applications.

3.2.5. *Freeze-thaw resistance*

The effect of wet density on the mass change of LFC after freeze-thaw cycles is presented in Fig. 25a. As can be seen, the mass loss is always negative, indicating an increase in the mass of LFC. And the mass variation decreases with wet density, resulting from differences in water absorption (Zhou and Su, 2023). The mass change of each mix is lower than 4% after 30 cycles, illustrating the mass stability of LFC. Fig. 25b shows the influence of wet density on the compressive strength. The strength of LFC increases at low number of cycles. After 5 cycles, the strength of D700S50 increases by 5.35%. The continuous cement hydration and pozzolanic reaction are responsible for this. The strength loss gradually increases with cycles. After 30 cycles, the strength of

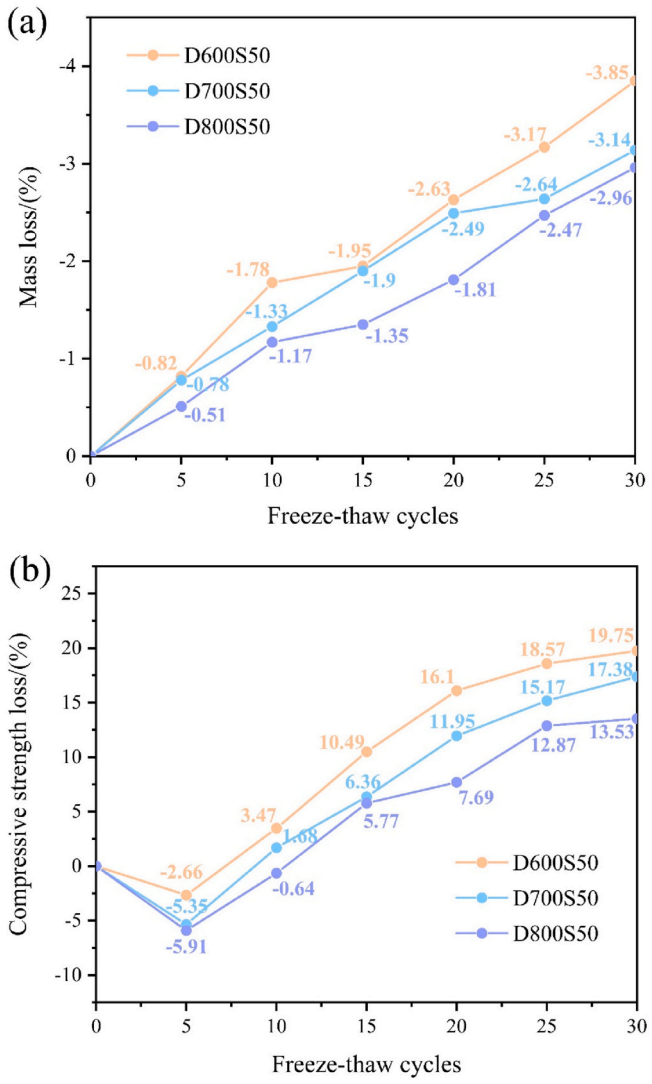

Fig. 25. The effect of wet density on mass (a) and compressive strength (b) of LFC under freeze-thaw cycles.

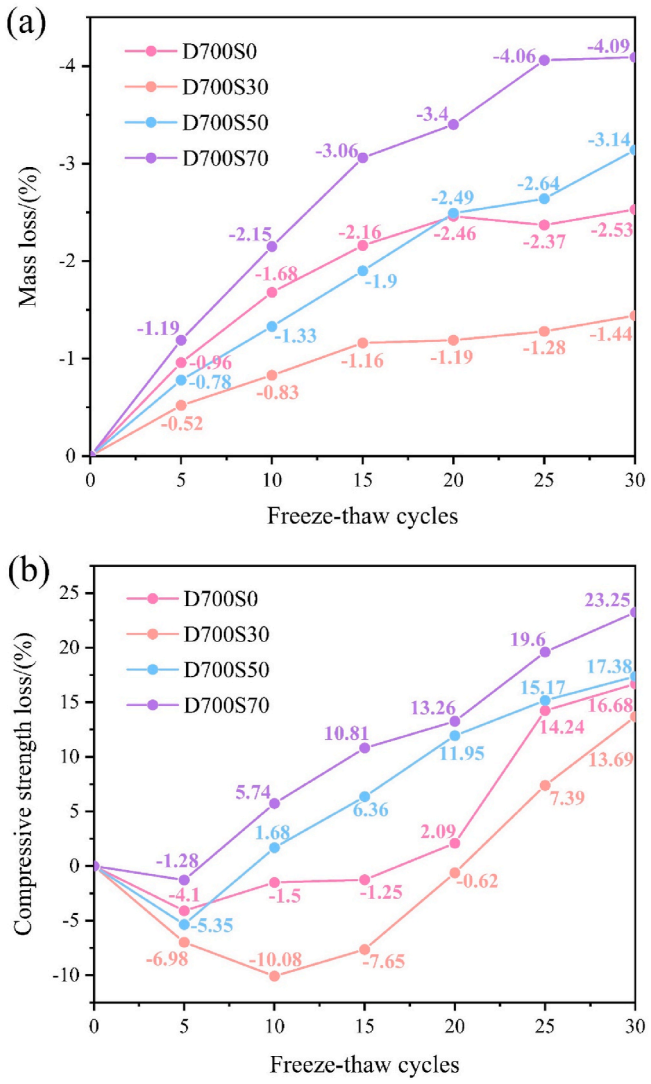

Fig. 26. The effect of GCFBFA substitution ratio on mass (a) and compressive strength (b) of LFC under freeze-thaw cycles.

D700S50 decreases by 17.38%. There are two reasons. On one side, under freezing conditions, the expansion of the frozen water damages the structure of LFC, connecting the air-voids and forming cracks (Vo and Park, 2016). On the other side, the temperature stress promotes the formation and development of cracks in LFC (Jin et al., 2020). As illustrated, the strength loss decreases with wet density increasing. After 30 cycles, the strength loss of D600S50, D700S50 and D800S50 is 19.75%, 17.38% and 13.53%, respectively. Because higher density LFC absorbs less water which results in less freeze-thaw damage (Zhang et al., 2024). Similar conclusion was reported by Wang et al. (2024b) that higher strength LFC typically survives more freeze-thaw cycles.

Fig. 26a shows the effect of GCFBFA on the mass. It is similar to that of LFC submerged in water. Compared with D700S0, the mass change ratio of D700S30 decreases, and that of D700S70 increases. After 30 cycles, the maximum mass change is within 5%, indicating the satisfactory mass stability. Fig. 26b shows the influence of GCFBFA substitution ratio on strength. The incorporation of 30% GCFBFA decreases the strength loss ratio, elaborating the improving effect of a better air system on the freeze-thaw resistance (Song et al., 2024). The strength loss ratio of D700S0 is 16.68%, and that of D700S30 is the lowest (13.69%), after 30 cycles. The strength losses of D700S0, D700S30 and D700S50 are under 20%, indicating favorable frost resistance.

Fig. 27 shows the surface change of LFC specimen after different number of freeze-thaw cycles. No cracking or spalling occurs on the surface of specimens, and only slight damage appears at the edges. This is consistent with the mass change of LFC. Besides, the strength loss of each LFC after 30 cycles is above 10%. This suggests that the strength change of LFC with increasing number of cycles is related to the deterioration of internal air-void structure and the formation of microcracks (Zhou and Su, 2023).

3.2.6. *Life cycle assessment*

A summary of LCA results for producing 1 m^3 LFC is given in Table 8. The environmental impact assessment focuses on the GWP and total cumulative energy consumption. As illustrated in the table, the GWP of D600S50 is 231.63 kg/m^3, while that of D700S50 and D800S50 increase by 29.89 and 59.78 kg/m^3, respectively. The total cumulative energy demand follows a similar trend to GWP with density. The GWP and total cumulative energy demand tend to increase with the wet density, as such increase is associated with an increase in the binder (Yang et al., 2014).

With increase of GCFBFA substitution ratio, the GWP decreases significantly. The largest GWP is from the D700S0, which is 419.87 kg/m^3. Compared with D700S0, the GWP of D700S30, D700S50, and D700S70 decrease by 23.4%, 37.7%, and 52.3%, respectively. The decarbonization of limestone in the sintering process of cement clinker

Fig. 27. The surface condition of LFC after different number of freeze-thaw cycles.

Table 8
LCA results for the production of 1 m^3 LFC.

Mix	Global warming potential (kg CO_2)	Total cumulative energy demand (GJ)
D700S0	419.87	2.94
D700S30	321.61	2.49
D700S50	261.52	2.07
D700S70	200.16	1.67
D600S50	231.63	1.89
D800S50	291.41	2.25

and the chemical fuel combustion which heats cement clinker to above 1200 °C results in the high GWP and energy consumption (Nie et al., 2022; Sousa and Bogas, 2021). However, CFBFA was reported to have a lower GWP and energy consumption due to the high combustion efficiency of CFB technology accompanied by a temperature requirement of lower than 1000 °C (Guo et al., 2024; Yoon et al., 2023). Thus, the total cumulative energy demand is reduced by 15.3% for D700S30, 29.6% for D700S50, and 43.2% for D700S70, compared to that of D700S0. In conclusion, GCFBFA-cement LFC may noteworthy be regarded as a sustainable engineering material in review of the significantly reduced GWP and energy consumption.

4. Conclusions

In the present study, GCFBFA is utilized as an SCM to prepare low-carbon LFC. The conclusions can be summarized as follows.

(1) The main reaction that occurs between GCFBFA and cement is the pozzolanic reaction, and the sulfate in GCFBFA promotes the generation of AFt. The binder incorporated with 30% GCFBFA achieves the greatest strength and the highest reaction degree, producing the most hydration products.
(2) GCFBFA retards cement hydration, prolongs setting time, reduces total hydration heat, and increases the heat release per gram of cement. Besides, GCFBFA increases the plastic viscosity of binder. And the yield stress is the highest at the substitution ratio of 30%. It is related to the ability of the slurry to confine the foam and therefore affects the air-void structure of LFC.
(3) Flowability of LFC increases with wet density and decreases with GCFBFA substitution ratio, which is within the required range of 160–190 mm. The mechanical properties of LFC can be optimized through the incorporation of an appropriate ratio (30%) of GCFBFA. The strength of LFC with wet density of 600 kg/m^3 and GCFBFA substitution ratio of 70% is the lowest, which still meets the requirement (0.8 MPa) of subgrade filling.
(4) Replacement of 30% cement by GCFBFA enhances the stability of fresh LFC slurry, reduces the air-void volume, equivalent diameter, and increase the sphericity, thus improving the air-void structure of LFC. However, incorporating too much GCFBFA (70%) achieves the opposite effect. In addition, the air-void characteristic parameters are significantly related to the compressive strength.
(5) The optimum GCFBFA substitution ratio for water stability is 50% and for freeze-thaw resistance is 30%. After soaking for 180 days, the water absorption ranges from 20% to 35%, and the compressive strength increases by more than 15%. Undergoing 30 freeze-thaw cycles, the mass change is under 5%, with a strength loss below 20% for all mixes expect the one with 70% GCFBFA substitution ratio.
(6) The life cycle assessment demonstrates the beneficial effect of utilizing GCFBFA as a substitute to cement for preparing low-carbon LFC. Incorporation of 70% GCFBFA reduces the global warming potential and total cumulative energy consumption of LFC preparation by 52.3% and 43.2%, respectively.

CRediT authorship contribution statement

Hongzhi Zhang: Writing – review & editing, Supervision, Funding acquisition, Conceptualization. **Quping Liang:** Writing – original draft, Methodology, Data curation. **Mingyang Shao:** Writing – review & editing. **Nengdong Jiang:** Resources, Investigation. **Wenqiang Ma:** Writing – review & editing. **Zhi Ge:** Writing – review & editing, Project administration. **Branko Šavija:** Writing – review & editing.

Declaration of competing interest

The authors declare that they have no known competing financial interests or personal relationships that could have appeared to influence the work reported in this paper.

Acknowledgements

This work was supported by Key Basic Research Project of China (No. 2022YFC3005604), National Natural Science Foundation of China (52378250), 111 Project (No. B21012), Taishan Scholar Foundation of Shandong Province (No. tsqn201909032) and "Unveiling and Commanding" Project of Jinan Municipal Bureau of Science and Technology (202323007).

Data availability

Data will be made available on request.

References

Aravind, N.R., Sathyan, D., Mini, K.M., 2020. Rice husk incorporated foam concrete wall panels as a thermal insulating material in buildings. Indoor Built Environ. 29, 721–729. https://doi.org/10.1177/1420326x19862017.
Awoyera, P.O., Britto, B.F., 2020. Foamed concrete incorporating mineral admixtures and pulverized ceramics: effect of phase change and mineralogy on strength characteristics. Construct. Build. Mater. 234. https://doi.org/10.1016/j.conbuildmat.2019.117434.
Chen, K.L., Lin, W.T., Liu, W.D., 2020. Microstructures and mechanical properties of sodium-silicate-activated slag/co-fired fly ash acementless composites. J. Clean. Prod. 277. https://doi.org/10.1016/j.jclepro.2020.124025.
Cheng, Y., Wang, X.Y., Chen, J.Z., Yu, H., Shen, J., Luo, X.G., Li, J.G., 2023. The performance of bubble-mixed lightweight soil to relieve expansion of circulating fluidized-bed fly ash. J. Build. Eng. 77. https://doi.org/10.1016/j.jobe.2023.107470.
Cheng, Z., He, L., Liu, L., Cheng, Z.J., Pei, X.B., Ma, Z., 2020. Mechanical properties and durability of high-performance concretes blended with circulating fluidized bed combustion ash and slag as replacement for ordinary Portland cement. Adv. Mater. Sci. Eng. https://doi.org/10.1155/2020/8613106, 2020.
Cho, S.W., Na, H.W., Hyung, W.G., 2021. Properties of Cement Mortar According to Mixing of Circulating Fluidized Bed Fly Ash and Pulverized Coal Fly Ash based on Blast Furnace Slag. J. Korea Inst. Build. Constr. 21, 141–148. https://doi.org/10.5345/JKIBC.2021.21.2.141.
Du, X.Q., Huang, Z., Ding, Y., Xu, W., Zhang, M., Wei, L.B., Yang, H.R., 2022. Feasibility study of grinding circulating fluidized bed ash as cement admixture. Materials 15. https://doi.org/10.3390/ma15165610.
Duan, S.Y., Liao, H.Q., Ma, Z.B., Cheng, F.Q., Fang, L., Gao, H.Y., Yang, H.Q., 2018. The relevance of ultrafine fly ash properties and mechanical properties in its fly ash-cement gelation blocks via static pressure forming. Construct. Build. Mater. 186, 1064–1071. https://doi.org/10.1016/j.conbuildmat.2018.08.035.
Falliano, D., De Domenico, D., Sciarrone, A., Ricciardi, G., Restuccia, L., Tulliani, J.M.C., Gugliandolo, E., 2019. Fracture behavior of lightweight foamed concrete: the crucial role of curing conditions. Theor. Appl. Fract. Mech. 103. https://doi.org/10.1016/j.tafmec.2019.102297.
Ge, Z., Yuan, H., Sun, R., Zhang, H., Wang, W., Qi, H., 2020. Use of green calcium sulphoaluminate cement to prepare foamed concrete for road embankment: a feasibility study. Construct. Build. Mater. 237. https://doi.org/10.1016/j.conbuildmat.2019.117791.
Gencel, O., Bilir, T., Bademler, Z., Ozbakkaloglu, T., 2022. A detailed review on foam concrete composites: ingredients, properties, and microstructure. Appl. Sci.-Basel 12. https://doi.org/10.3390/app12115752.
Golaszewska, M., Giergiczny, Z., 2021. Study of the properties of blended cements containing various types of slag cements and limestone powder. Materials 14. https://doi.org/10.3390/ma14206072.
Guo, W., Yao, W., Liang, G., Shi, C., She, A., Wei, Y., 2024. Mechanical properties, microstructure and life-cycle assessment of eco-friendly cementitious materials containing circulating fluidized bed fly ash and ground granulated blast furnace slag. J. Build. Eng. 95, 110293. https://doi.org/10.1016/j.jobe.2024.110293.

Gupta, S., Chaudhary, S., 2022. State of the art review on supplementary cementitious materials in India – II: characteristics of SCMs, effect on concrete and environmental impact. J. Clean. Prod. 357, 131945. https://doi.org/10.1016/j.jclepro.2022.131945.
Han, F., Pu, S., Zhou, Y., Zhang, H., Zhang, Z., 2022. Effect of ultrafine mineral admixtures on the rheological properties of fresh cement paste: a review. J. Build. Eng. 51, 104313. https://doi.org/10.1016/j.jobe.2022.104313.
He, P.Y., Zhang, X.M., Chen, H., Zhang, Y.J., 2021. Waste-to-resource strategies for the use of circulating fluidized bed fly ash in construction materials: a mini review. Powder Technol. 393, 773–785. https://doi.org/10.1016/j.powtec.2021.08.035.
Hilal, A.A., Thom, N.H., Dawson, A.R., 2015. On void structure and strength of foamed concrete made without/with additives. Construct. Build. Mater. 85, 157–164. https://doi.org/10.1016/j.conbuildmat.2015.03.093.
Hou, L., Li, J., Lu, Z.Y., Niu, Y.H., Jiang, J., Li, T.Z., 2019. Effect of nanoparticles on foaming agent and the foamed concrete. Construct. Build. Mater. 227. https://doi.org/10.1016/j.conbuildmat.2019.116698.
Ji, Z., Zhang, G., Chen, Y., Liu, R., Qu, J., Liu, H., 2023. Synchronous recycling of multi-source solid wastes for low-carbon geopolymer preparation: primary factors identification and feasibility assessment. J. Clean. Prod. 430, 139633. https://doi.org/10.1016/j.jclepro.2023.139633.
Ji, Z., Zhang, G., Liu, R., Qu, J., Liu, H., 2024. Potential applications of solid waste-based geopolymer materials: in wastewater treatment and greenhouse gas emission reduction. J. Clean. Prod. 443, 141144. https://doi.org/10.1016/j.jclepro.2024.141144.
Jia, G.H., Wang, Y.L., Yang, F.L., 2022. A review on the application of circulating fluidized bed fly ash in building materials. Adv. Mater. Sci. Eng. 2022. https://doi.org/10.1155/2022/7099430.
Jiang, L.B., Wang, Z., Wang, Y., Niu, J.H., Qin, J.H., 2024. Preparation and properties of carbon dioxide foamed concrete using nanoparticles as foam stabilizer and pre-carbonated cement slurry. Cem. Concr. Compos. 151. https://doi.org/10.1016/j.cemconcomp.2024.105585.
Jiang, N., Ge, Z., Guan, Y., Zuo, Z., Zhang, H., Ling, Y., Šavija, B., 2022. Experimentally validated meso-scale fracture modelling of foamed concrete. Theor. Appl. Fract. Mech. 122. https://doi.org/10.1016/j.tafmec.2022.103631.
Jin, S.S., Zheng, G.P., Yu, J., 2020. A micro freeze-thaw damage model of concrete with fractal dimension. Construct. Build. Mater. 257. https://doi.org/10.1016/j.conbuildmat.2020.119434.
John, E., Lothenbach, B., 2023. Cement hydration mechanisms through time - a review. J. Mater. Sci. 58, 9805–9833. https://doi.org/10.1007/s10853-023-08651-9.
Karakurt, C., Kurama, H., Topçu, I.B., 2010. Utilization of natural zeolite in aerated concrete production. Cem. Concr. Compos. 32, 1–8. https://doi.org/10.1016/j.cemconcomp.2009.10.002.
Le, T.H.M., Lee, T.W., Seo, J.W., Park, D.W., 2022. Feasibility study of locally excavated soil in foamed cement mixture as backfill material for abutments of railway bridges. J. Test. Eval. 50, 2967–2987. https://doi.org/10.1520/jte20210169.
Li, D.L., Sun, R., Wang, D.M., Ren, C.F., Fang, K.Z., 2021a. Study on the pozzolanic activity of ultrafine circulating fluidized-bed fly ash prepared by jet mill. Fuel 291. https://doi.org/10.1016/j.fuel.2021.120220.
Li, J.W., Chen, Z.C., Li, L.K., Qiao, Y.Y., Yuan, Z.H., Zeng, L.Y., Li, Z.Q., 2021b. Study on pore and chemical structure characteristics of atmospheric circulating fluidized bed coal gasification fly ash. J. Clean. Prod. 308. https://doi.org/10.1016/j.jclepro.2021.127395.
Li, Z., Yuan, H., Gao, F., Zhang, H., Ge, Z., Wang, K., Sun, R., Guan, Y., Ling, Y., Jiang, N., 2021c. A feasibility study of low cement content foamed concrete using high volume of waste lime mud and fly ash for road embankment. Materials 15. https://doi.org/10.3390/ma15010086.
Liu, G., Wang, J., 2024. Utilization of carbonated alkaline solid wastes in ordinary Portland cement-metakaolin-limestone ternary mixture: underlying the role of low grade-sustainable calcium carbonate sources. J. Clean. Prod. 456, 142382. https://doi.org/10.3390/ma15010086.
Liu, W., Liu, X., Zhang, L., Wan, Y., Li, H., Jiao, X., 2024. Rheology, mechanics, microstructure and durability of low-carbon cementitious materials based on circulating fluidized bed fly ash: a comprehensive review. Construct. Build. Mater. 411, 134688. https://doi.org/10.1016/j.conbuildmat.2023.134688.
Liu, Z., Li, L., Shao, N.N., Hu, T., Han, L., Wang, D.M., 2020. Geopolymerization enhanced hydrothermal synthesis of analcime from steel slag and CFBC fly ash and heavy metal adsorption on analcime. Environ. Technol. 41, 1753–1765. https://doi.org/10.1080/09593330.2018.1545805.
Makul, N., Sua-iam, G., 2016. Characteristics and utilization of sugarcane filter cake waste in the production of lightweight foamed concrete. J. Clean. Prod. 126, 118–133. https://doi.org/10.1016/j.jclepro.2016.02.111.
Mbasha, W., Haldenwang, R., Masalova, I., 2020. The influence of sulfate availability on rheology of fresh cement paste. Appl. Rheol. 30, 54–63. https://doi.org/10.1515/arh-2020-0106.
Nambiar, E.K.K., Ramamurthy, K., 2007. Air-void characterisation of foam concrete. Cement Concr. Res. 37, 221–230. https://doi.org/10.1016/j.cemconres.2006.10.009.
Narayanan, N., Ramamurthy, K., 2000. Structure and properties of aerated concrete: a review. Cem. Concr. Compos. 22, 321–329. https://doi.org/10.1016/S0958-9465(00)00016-0.
Nie, S., Zhou, J., Yang, F., Lan, M., Li, J., Zhang, Z., Chen, Z., Xu, M., Li, H., Sanjayan, J. G., 2022. Analysis of theoretical carbon dioxide emissions from cement production: Methodology and application. J. Clean. Prod. 334, 130270. https://doi.org/10.1016/j.jclepro.2021.130270.
Ohenoja, K., Körkkö, M., Wigren, V., Österbacka, J., Illikainen, M., 2019. Increasing the utilization potential of fly ashes from fluidized bed combustion by mechanical treatments. Int. J. Enviro. Sci. Technol. 16, 1839–1846. https://doi.org/10.1007/s13762-018-1812-x.
Othman, R., Jaya, R.P., Muthusamy, K., Sulaiman, M., Duraisamy, Y., Abdullah, M.M.A., Przybyl, A., Sochacki, W., Skrzypczak, T., Vizureanu, P., Sandu, A.V., 2021. Relation between density and compressive strength of foamed concrete. Materials 14. https://doi.org/10.3390/ma14112967.
Paaver, P., Paiste, P., Liira, M., Kirsimäe, K., 2021. Mechanical activation of the Ca-rich circulating fluidized bed combustion fly ash: development of an alternative binder system. Minerals 11. https://doi.org/10.3390/min11010003.
Qi, X.Q., Bao, Y.F., Wang, W.R., Zhang, S.L., Wu, Y.L., Jia, Z.Q., Guo, S.Y., 2024. Superior performance foamed concrete fabricated with amphiphilic and hydrophilic particles stabilized ultra-stable foam. Cem. Concr. Compos. 152. https://doi.org/10.1016/j.cemconcomp.2024.105613.
Raj, A., Sathyan, D., Mini, K.M., 2019. Physical and functional characteristics of foam concrete: a review. Construct. Build. Mater. 221, 787–799. https://doi.org/10.1016/j.conbuildmat.2019.06.052.
Schneider, M., Hoenig, V., Ruppert, J., Rickert, J., 2023. The cement plant of tomorrow. Cement Concr. Res. 173, 107290. https://doi.org/10.1016/j.cemconres.2023.107290.
Shah, S.N., Mo, K.H., Yap, S.P., Yang, J., Ling, T.-C., 2021. Lightweight foamed concrete as a promising avenue for incorporating waste materials: a review. Resour. Conserv. Recycl. 164. https://doi.org/10.1016/j.resconrec.2020.105103.
Shen, G., 2009. Character of the circulating fluidized bed boiler fly ash and the application in cement industry. Cem. Eng. 79–82. https://doi.org/10.3969/j.issn.1007-0389.2009.05.026.
Shi, J.Y., Liu, B.J., He, Z.H., Liu, Y.C., Jiang, J.Y., Xiong, T.Y., Shi, J.W., 2021. A green ultra-lightweight chemically foamed concrete for building exterior: a feasibility study. J. Clean. Prod. 288. https://doi.org/10.1016/j.jclepro.2020.125085.
Song, Q., Zhang, P., Bao, J., Xue, S., Mu, S., Han, X., 2021. Research progress and application of foam concrete. J. Chin. Ceram. Soc. 49, 398–410. https://doi.org/10.14062/j.issn.0454-5648.20200316.
Song, Y.P., Xue, C.H., Guo, W.C., Bai, Y.Y., Shi, Y.X., Zhao, Q.X., 2024. Foamed geopolymer insulation materials: Research progress on insulation performance and durability. J. Clean. Prod. 444. https://doi.org/10.1016/j.jclepro.2024.140991.
Sousa, V., Bogas, J.A., 2021. Comparison of energy consumption and carbon emissions from clinker and recycled cement production. J. Clean. Prod. 306, 127277. https://doi.org/10.1016/j.jclepro.2021.127277.
Sun, Z.N., Tan, X.J., Chen, W.Z., Mu, R., 2022. Chemical shrinkage of ferrite-rich calcium sulfoaluminate clinkers with varied gypsum contents. Construct. Build. Mater. 357. https://doi.org/10.1016/j.conbuildmat.2022.128729.
Thiyagarajan, H., Mungule, M., Sasmal, S., 2022. Micro aggregate and pozzolanic reactivity of fly ash: effect on fracture properties. Aust. J. Civ. Eng. https://doi.org/10.1080/14488353.2022.2145030.
Tran, N.P., Nguyen, T.N., Ngo, T.D., Le, P.K., Le, T.A., 2022. Strategic progress in foam stabilisation towards high-performance foam concrete for building sustainability: a state-of-the-art review. J. Clean. Prod. 375. https://doi.org/10.1016/j.jclepro.2022.133939.
Vo, H.V., Park, D.W., 2016. Lightweight treated soil as a potential sustainable pavement material. J. Perform. Constr. Facil. 30. https://doi.org/10.1061/(asce)cf.1943-5509.0000720.
Vu, C.C., Weiss, J., Plé, O., Amitrano, D., 2021. The potential impact of size effects on compressive strength for the estimation of the Young's modulus of concrete. Mater. Struct. 54. https://doi.org/10.1617/s11527-021-01795-7.
Wagh, C.D., Gandhi, I.S.R., 2024. Investigations on the performance of xanthan gum as a foam stabilizer and assessment of economic and environmental impacts of foam concrete production. J. Build. Eng. 82, 108286. https://doi.org/10.1016/j.jobe.2023.108286.
Wallevik, O.H., Feys, D., Wallevik, J.E., Khayat, K.H., 2015. Avoiding inaccurate interpretations of rheological measurements for cement-based materials. Cement Concr. Res. 78, 100–109. https://doi.org/10.1016/j.cemconres.2015.05.003.
Wang, J., Ren, C., Huang, T., Li, X., Cao, W., Zhu, Y., Wei, P., Wang, D., Liu, Z., 2024a. Performances of concrete with binder and/or aggregates replacement by all-solid waste materials. J. Clean. Prod. 450, 141929. https://doi.org/10.1016/j.jclepro.2024.141929.
Wang, L., Yang, H.Q., Dong, Y., Chen, E., Tang, S.W., 2018a. Environmental evaluation, hydration, pore structure, volume deformation and abrasion resistance of low heat Portland (LHP) cement-based materials. J. Clean. Prod. 203, 540–558. https://doi.org/10.1016/j.jclepro.2018.08.281.
Wang, R., Gao, P.W., Tian, M.H., Dai, Y.C., 2019. Experimental study on mechanical and waterproof performance of lightweight foamed concrete mixed with crumb rubber. Construct. Build. Mater. 209, 655–664. https://doi.org/10.1016/j.conbuildmat.2019.03.157.
Wang, S.B., Chen, C.L., Kadum, M.J., Shiau, B.J., Harwell, J.H., 2018b. Enhancing foam stability in porous media by applying nanoparticles. J. Dispersion Sci. Technol. 39, 734–743. https://doi.org/10.1080/01932691.2017.1388175.
Wang, X., Huang, J., Dai, S.B., Ma, B.G., Jiang, Q., 2020. Investigation of silica fume as foam cell stabilizer for foamed concrete. Construct. Build. Mater. 237. https://doi.org/10.1016/j.conbuildmat.2019.117514.
Wang, X., Li, S., Zhou, A., Liu, R., Duan, S., Wang, M., 2021. Influence of the bleeding characteristic on density and rheology in cement slurry. Construct. Build. Mater. 269, 121316. https://doi.org/10.1016/j.conbuildmat.2020.121316.
Wang, Z.C., Liu, S.Y., Wu, K., Li, M.Y., Zhang, X., Huang, L., 2024b. Durability against dry-wet and freeze-thaw cycles of alkali residue-based foamed concrete. Mater. Struct. 57. https://doi.org/10.1617/s11527-024-02318-w.

Xia, Y., Yan, Y., Hu, Z., 2013. Utilization of circulating fluidized bed fly ash in preparing non-autoclaved aerated concrete production. Construct. Build. Mater. 47, 1461–1467. https://doi.org/10.1016/j.conbuildmat.2013.06.033.

Xiong, Y.L., Zhang, Z.D., Zhang, C., Xiao, J.C., 2024. Foam-stability enhancement in biochar-infused foam concrete: analyzing ionic strength, interparticle distance, and water state. J. Clean. Prod. 443. https://doi.org/10.1016/j.jclepro.2024.141231.

Yang, K.-H., Lee, K.-H., Song, J.-K., Gong, M.-H., 2014. Properties and sustainability of alkali-activated slag foamed concrete. J. Clean. Prod. 68, 226–233. https://doi.org/10.1016/j.jclepro.2013.12.068.

Yang, W., Li, B., Ma, W., 2022. Experimental study on reducing water absorption of air-foam treated lightweight soil. J. Disaster Prev. Mitig. Eng. 42, 1061–1068. https://doi.org/10.13409/j.cnki.jdpme.20210307001.

Yang, X.Y., Zhao, L., Haque, M.A., Chen, B., Ren, Z., Cao, X.D., Shen, Z.M., 2020. Sustainable conversion of contaminated dredged river sediment into eco-friendly foamed concrete. J. Clean. Prod. 252. https://doi.org/10.1016/j.jclepro.2019.119799.

Yao, T., Tian, Q., Zhang, M., Qi, S., Wang, C., Ruan, M., 2023a. Laboratory investigation of foamed concrete prepared by recycled waste concrete powder and ground granulated blast furnace slag. J. Clean. Prod. 426, 139095. https://doi.org/10.1016/j.jclepro.2023.139095.

Yao, T.S., Tian, Q., Zhang, M., Qi, S., Wang, C., Ruan, M.Y., 2023b. Laboratory investigation of foamed concrete prepared by recycled waste concrete powder and ground granulated blast furnace slag. J. Clean. Prod. 426. https://doi.org/10.1016/j.jclepro.2023.139095.

Yao, X., Wang, W., Liu, M., Yao, Y., Wu, S., 2019. Synergistic use of industrial solid waste mixtures to prepare ready-to-use lightweight porous concrete. J. Clean. Prod. 211, 1034–1043. https://doi.org/10.1016/j.jclepro.2018.11.252.

Yin, J., Li, D., Wang, D., Lin, H., Cui, Y., 2015. Effect of mineral admixture on properties of large volume of circulating fluidized bed fly ash cement. Non-met. Min. 38, 37–40. https://doi.org/10.3969/j.issn.1000-8098.2015.05.012.

Yoon, S.H., Kim, S.-J., Baek, G.-U., Moon, J.H., Jo, S.H., Park, S.J., Kim, J.-Y., Yoon, S.-J., Ra, H.W., Yoon, S.-M., Lee, J.G., Kim, J.-S., Mun, T.-Y., 2023. Operational optimization of air staging and flue gas recirculation for NOx reduction in biomass circulating fluidized bed combustion. J. Clean. Prod. 387, 135878. https://doi.org/10.1016/j.jclepro.2023.135878.

Yuan, H., Ge, Z., Sun, R., Xu, X., Lu, Y., Ling, Y., Zhang, H., 2022. Drying shrinkage, durability and microstructure of foamed concrete containing high volume lime mud-fly ash. Construct. Build. Mater. 327. https://doi.org/10.1016/j.conbuildmat.2022.126990.

Yuan, Q., Zhang, K., Huang, T., Liu, X., Wang, Y., 2024. Rheological behaviors evolution and setting mechanism of magnesium oxychloride cement paste. Construct. Build. Mater. 440. https://doi.org/10.1016/j.conbuildmat.2024.137506.

Zahedi, M., Rajabipour, F., 2019. Fluidized bed combustion (FBC) fly ash and its performance in concrete. ACI Mater. J. 116, 163–172. https://doi.org/10.14359/51716720.

Zhang, C., Liu, R., Chen, M., Li, J., Wang, X., Liu, Y., Zhu, Z., Wang, M., Fan, F., 2022a. Influence of the flocculation effect on the rheological properties of cement slurry. Powder Technol. 398, 117118. https://doi.org/10.1016/j.powtec.2022.117118.

Zhang, C., Wang, M., Liu, R., Li, X., Liu, Y., Jiang, P., Yan, J., Zhu, Z., Chen, M., 2023a. Rheological properties of cement-based slurry and evaluation of rheological model: influence of particle size and shape. Construct. Build. Mater. 406, 133498. https://doi.org/10.1016/j.conbuildmat.2023.133498.

Zhang, H.B., Wang, J., Liu, Z.K., Ma, C.Y., Song, Z.S., Cui, F., Wu, J.Q., Song, X.G., 2024. Strength characteristics of foamed concrete under coupling effect of constant compressive loading and freeze-thaw cycles. Construct. Build. Mater. 411. https://doi.org/10.1016/j.conbuildmat.2023.134565.

Zhang, J., Scherer, G.W., 2011. Comparison of methods for arresting hydration of cement. Cement Concr. Res. 41, 1024–1036. https://doi.org/10.1016/j.cemconres.2011.06.003.

Zhang, W., Gu, J., Zhou, X., Li, Y., Wang, Y., Xue, Y., Liu, X., 2021. Circulating fluidized bed fly ash based multi-solid wastes road base materials: hydration characteristics and utilization of SO_3 and f -CaO. J. Clean. Prod. 316, 128355. https://doi.org/10.1016/j.jclepro.2021.128355.

Zhang, W., Liu, X., Zhang, Z., 2022b. Mechanical, expansion and rheological properties of circulating fluidized bed fly ash based ecological cement: a critical review. Int. J. Miner. Metall. Mater. 29, 1670–1682. https://doi.org/10.1007/s12613-021-2403-2.

Zhang, W., Liu, X.M., Zhang, Z.Q., Li, Y.T., Gu, J.R., Wang, Y.G., Xue, Y., 2022c. Circulating fluidized bed fly ash-blast furnace slag based cementitious materials: hydration behaviors and performance. Construct. Build. Mater. 342. https://doi.org/10.1016/j.conbuildmat.2022.128006.

Zhang, Z., Li, X., Wang, H., Yuan, J., Jin, S., Yan, T., 2023c. Research progress on influence of fly ash characteristics on occurrence and migration of heavy metals in circulating fluidized bed. Appl. Chem. Ind. 52, 3205–3209. https://doi.org/10.3969/j.issn.1671-3206.2023.11.046.

Zhao, J.H., Li, D.L., Liao, S.C., Wang, D.M., Wang, H., Yan, P.Y., 2018. Influence of mechanical grinding on pozzolanic characteristics of circulating fluidized bed fly ash (CFA) and resulting consequences on hydration and hardening properties of blended cement. J. Therm. Anal. Calorim. 132, 1459–1470. https://doi.org/10.1007/s10973-018-7103-4.

Zheng, D.-p., Wang, D.-m., Li, D.-l., Ren, C.-f., Tang, W.-c., 2017. Study of high volume circulating fluidized bed fly ash on rheological properties of the resulting cement paste. Construct. Build. Mater. 135, 86–93. https://doi.org/10.1016/j.conbuildmat.2016.12.127.

Zheng, D.P., Wang, D.M., Cui, H.Z., Chen, X.S., 2023. Hydration characteristics of cement with high volume circulating fluidized bed fly ash. Construct. Build. Mater. 380. https://doi.org/10.1016/j.conbuildmat.2023.131310.

Zhou, D.D., Gao, H.Y., Liao, H.Q., Fang, L., Cheng, F.Q., 2021. Enhancing the performance of foam concrete containing fly ash and steel slag via a pressure foaming process. J. Clean. Prod. 329. https://doi.org/10.1016/j.jclepro.2021.129664.

Zhou, G.Z., Su, R.K.L., 2023. A review on durability of foam concrete. Buildings 13. https://doi.org/10.3390/buildings13071880.

Zhou, M.K., Chen, P., Chen, X., Ge, X.X., Wang, Y.Q., 2020. Study on hydration characteristics of circulating fluidized bed combustion fly ash (CFBCA). Construct. Build. Mater. 251. https://doi.org/10.1016/j.conbuildmat.2020.118993.

Zhou, Y., Pu, S., Han, F., Zhang, H., Zhang, Z., 2022. Effect of ultrafine slag on hydration heat and rheology properties of Portland cement paste. Powder Technol. 405. https://doi.org/10.1016/j.powtec.2022.117549.

Zhu, C., Dong, B., Lazorenko, G., Fang, G., Wang, Y., Zuo, J., 2024. Sandy soil based foam concrete with ultra-small pore structure through in-situ mechanical frothing. J. Build. Eng. 91, 109675. https://doi.org/10.1016/j.jobe.2024.109675.